TURBULENT MIXING IN THE SURFACE LAYERS OF ACCRETING NEUTRON STARS

Anthony L. Piro[1] and Lars Bildsten
Kavli Institute for Theoretical Physics, University of California, Santa Barbara, CA 93106; piro@kitp.ucsb.edu, bildsten@kitp.ucsb.edu

ABSTRACT

During accretion, a neutron star (NS) is spun up as angular momentum is transported through its surface layers. We study the resulting differentially rotating profile, focusing on the impact this has for type I X-ray bursts. The predominant viscosity is likely provided by the Tayler-Spruit dynamo, where toroidal magnetic field growth and Tayler instabilities balance to support a steady state magnetic field. The radial and azimuthal components have strengths of $\sim 10^5$ and $\sim 10^{10}$ G, respectively. This leads to nearly uniform rotation at the depths of X-ray bursts. A remaining small shear transmits the accreted angular momentum inward to the NS interior. Although this shear gives little viscous heating, it can trigger turbulent mixing. Detailed simulations will be required to fully understand the consequences of mixing, but our models illustrate some general features. Mixing has the greatest impact when the buoyancy at the compositional discontinuity between accreted matter and ashes is overcome. This occurs preferentially at high accretion rates or low spin frequencies and may depend on the ash composition from the previous burst. We then find two new regimes of burning. The first is ignition in a layer containing a mixture of heavier elements from the ashes. If ignition occurs at the base of the mixed layer, recurrence times as short as $\sim 5-30$ minutes are possible. This may explain the short recurrence time of some bursts, but incomplete burning is still needed to explain these bursts' energetics. When mixing is sufficiently strong, a second regime is found where accreted helium mixes deep enough to burn stably, quenching X-ray bursts. The carbon-rich material produced by stable helium burning would be important for triggering and fueling superbursts.

Subject headings: accretion, accretion disks — stars: magnetic fields — stars: neutron — X-rays: bursts — X-rays: stars

1. INTRODUCTION

As neutron stars (NSs) in low-mass X-ray binaries accrete material from their companions, they are expected to be spun up by this addition of angular momentum, possibly becoming millisecond pulsars (Bhattacharya & van den Heuvel 1991). This suspicion has received support by the discovery of accretion-driven millisecond pulsars (Wijnands & van der Klis 1998), as well as the millisecond oscillations seen during type I X-ray bursts (Chakrabarty et al. 2003), the unstable ignition of the accumulating fuel (for reviews, see Lewin et al. 1995; Strohmayer & Bildsten 2006; Galloway et al. 2006). The majority of the rotational kinetic energy of the accreted material is dissipated at low densities ($\sim 10^{-4}$ to 10^{-1} g cm^{-3}) in the boundary layer (e.g., Inogamov & Sunyaev 1999). Nevertheless, angular momentum must be transported into the NS interior if it is to be spun up, even if at times the angular momentum could be radiated as gravitational waves (Bildsten 1998b). This transport implies a nonzero, albeit small, shear throughout the outer liquid parts of the NS. Such shearing may lead to viscous heating as well as chemical mixing at depths far below the low-density boundary layer where the majority of the shearing occurs.

Such a picture was previously investigated by Fujimoto (1988, 1993) for both accreting NSs and white dwarfs. His studies demonstrated that the shearing profile of a NS could be large enough that mixing through baroclinic instabilities may be important at the depths of type I X-ray bursts. Such a result is compelling because it may help to explain some of the remaining discrepancies between the theory and observations of these bursts. Although a simple limit cycle picture has been successful in qualitatively

explaining the bursts' primary characteristics, including their energies ($10^{39}-10^{40}$ ergs), recurrence times (hours to days), and durations ($\sim 10-100$ s) (Fujimoto et al. 1981; Bildsten 1998a), outstanding problems still remain (Fujimoto et al. 1987; van Paradijs et al. 1988; Bildsten 2000). Chief among these is the critical accretion rate required for stable accumulation (which we discuss in more detail in § 6). Another problem is the occurrence of successive X-ray bursts with recurrence times as short as ~ 10 minutes (Galloway et al. 2006 and references therein), for which there has been speculation that this could be due to mixing during accretion (Fujimoto et al. 1987).

In this present work we reassess the importance of angular momentum transport and the resulting mixing. We find that the hydrodynamic instabilities studied by Fujimoto (1993) are insufficient to prevent strong shearing of magnetic fields. This leads to generation of the Tayler-Spruit dynamo (Spruit 2002), where toroidal field growth is balanced by Tayler instabilities to create a steady state magnetic field, which provides a torque on the shearing layers that is larger than any purely hydrodynamic mechanism. The result is nearly uniform rotation and little viscous heating, too little to affect either X-ray bursts or superbursts (thermonuclear ignition of ashes from previous X-ray bursts; Cumming & Bildsten 2001; Strohmayer & Brown 2002). Turbulent mixing is found to be nonnegligible and in some cases may mix fresh material with the ashes of previous bursts. The key is whether the strong buoyancy due to the larger density of the ashes below can be overcome. When mixing occurs, we find two new regimes of burning for an accreting NS. The first is that fuel can be mixed down to depths necessary for premature unstable ignition. The timescale for ignition of such bursts is short enough ($\sim 5-30$ minutes) to explain the short recurrence time bursts (Galloway et al. 2006). The second is that if material is mixed to sufficiently large depths (and therefore temperatures),

[1] Current address: Astronomy Department and Theoretical Astrophysics Center, University of California, Berkeley, CA 94720; tpiro@astro.berkeley.edu.
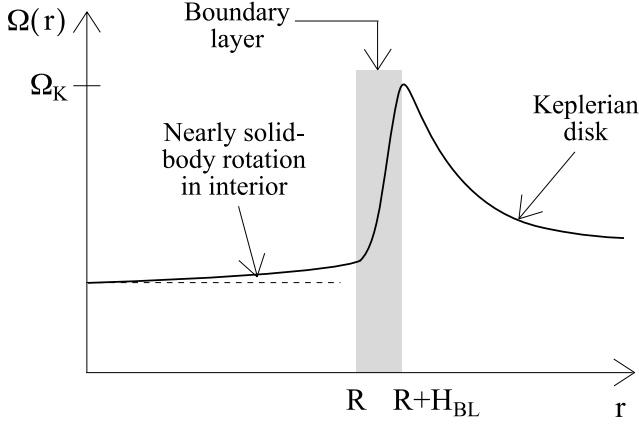
Fig. 1.—Diagram demonstrating the rotation profile of material from the accretion disk, through the boundary layer, and into the NS. Material reaches the NS surface with a Keplerian spin frequency Ω_K, the majority of which is dissipated within the boundary layer (*gray region*) with thickness $H_{BL} \ll R$. Nevertheless, angular momentum is still being added to the NS, and a torque must be communicated through the NS. This implies a small, nonzero amount of shear throughout the NS interior.

it can burn stably, ceasing X-ray bursts altogether. Such a mechanism may be responsible for the quenching of X-ray bursts seen at surprisingly low accretion rates for many atoll class NSs (Cornelisse et al. 2003). We derive an analytic formula that estimates what spins and accretion rates are necessary to transfer between these two regimes (eq. [77]).

1.1. *The Basics of Angular Momentum Transport*

Before beginning more detailed analysis, it is useful to present some general equations for angular momentum transport. This demonstrates why we expect the NS interior to be shearing and explicitly relates the torque from the accreting matter to this shear. Figure 1 schematically shows the expected rotation profile from the accretion disk, through the boundary layer, and into the NS interior. Material accreted at a rate $\dot{M}$ reaches the NS surface with a nearly Keplerian spin frequency of $\Omega_K = (GM/R^3)^{1/2} = 1.4 \times 10^4 \text{ s}^{-1} M_{1.4}^{1/2} R_6^{-3/2}$, where $M_{1.4} \equiv M/(1.4 \, M_\odot)$ and $R_6 \equiv R/(10^6 \text{ cm})$, which has a kinetic energy of ≈ 200 MeV nucleon^{-1}. The majority of this energy is dissipated in a boundary layer of thickness $H_{BL} \ll R$ (as studied by Inogamov & Sunyaev 1999) and never reaches far into the NS surface. Nevertheless, angular momentum is being added at a rate of $\dot{M}(GMR)^{1/2}$, so that a torque of this magnitude must be communicated into the NS. This implies a nonzero shear rate in the interior liquid layers, down to the solid crust. In the present work we are interested in the shear at the depths where X-ray bursts ignite, near $\rho \approx 10^6 \text{ g cm}^{-3}$, which is well below the boundary layer. Although we focus on a magnetic mechanism for angular momentum transport, we expect the boundary layer and densities up to $\approx 5 \times 10^3 \text{ g cm}^{-3}$ to be dominated by hydrodynamic instabilities (which we discuss in more detail in § 3).

The pressure scale height at the depth of X-ray bursts is $H \approx 30 \text{ cm} \ll R$, which allows us to use a Cartesian coordinate system with z as the radial coordinate. This is far below the depths considered by Inogamov & Sunyaev (1999) when they investigated the uneven covering of the NS surface by accreted fuel. Furthermore, all of the transport mechanisms we consider work most efficiently in directions perpendicular to gravity (because no work is performed); thus, it is a good approximation to consider the surface layers as concentric spheres, each with constant Ω.

Transfer of angular momentum is reduced to a one-dimensional diffusion equation (Fujimoto 1993)

$$\frac{d}{dt}\left(R^2\Omega\right) = \frac{1}{R^2\rho}\frac{\partial}{\partial z}\left(\rho\nu R^4 \frac{\partial\Omega}{\partial z}\right), \qquad (1)$$

where Ω is the NS spin frequency and ν is the viscosity. The total time derivative is given by $d/dt = \partial/\partial t + V_{adv}\partial/\partial z$, where V_{adv} is the advecting velocity of the fluid in an Eulerian frame. In steady state, we take $\partial/\partial t = 0$ and set $V_{adv} = -\dot{M}/(4\pi R^2\rho)$ so that

$$-\frac{\dot{M}}{4\pi R^2}\frac{d}{dz}\left(R^2\Omega\right) = \frac{1}{R^2}\frac{d}{dz}\left(\rho\nu R^4\frac{d\Omega}{dz}\right). \qquad (2)$$

Integrating from the surface where the spin is Ω_K (due to the disk) down to a depth z where the local spin is Ω and assuming $d\Omega/dz = 0$ at the surface,

$$-\dot{M}R^2\Omega_K + \dot{M}R^2\Omega = -4\pi\rho\nu R^4 \, d\Omega/dz. \qquad (3)$$

Taking the limit $\Omega \ll \Omega_K$, we find

$$4\pi R^3 \rho\nu q\Omega = \dot{M}R^2\Omega_K, \qquad (4)$$

where $q \equiv d\log\Omega/d\log z$ is the shear rate. This equation shows that $q > 0$ when angular momentum is transported inward. In general, we will find that q is rather small ($\lesssim 1$) at the depths of interest. Nevertheless, q is large enough to activate instabilities that help to transport angular momentum, as well as mix material.

1.2. *Outline of Paper*

We begin by comparing and contrasting some well-known hydrodynamic instabilities in § 2 and estimate the resulting shear rates. In § 3 we discuss the consequences that this shearing has on a magnetic field, which motivates implementation of the Tayler-Spruit dynamo. In § 4 we calculate accumulating NS envelopes without the effects of viscous angular momentum transport. This enables us to judge when such effects must be incorporated. We calculate models including mixing in § 5. We conclude in § 6 with a summary of our results and a discussion of type I X-ray burst and superburst observations.

2. HYDRODYNAMIC VISCOSITY MECHANISMS

In the following sections we discuss hydrodynamic instabilities. This is not an exhaustive survey (for further details, see Heger et al. 2000), but rather is meant to summarize those instabilities that are most crucial to our problem, so as to set the context for the magnetic transport mechanism we study later.

2.1. *Kelvin-Helmholtz Instability*

The Kelvin-Helmholtz instability (also referred to as the dynamical shear instability) is governed by the Richardson number

$$\text{Ri} \equiv \frac{N^2}{q^2\Omega^2}, \qquad (5)$$

where N is the Brunt-Väisälä frequency, which is composed of contributions from thermal and compositional buoyancy,

$$N^2 = N_T^2 + N_\mu^2. \qquad (6)$$

The thermal buoyancy is given by

$$N_T^2 = \frac{g}{H} \frac{\chi_T}{\chi_\rho} \left[\nabla_{\rm ad} - \left(\frac{d \ln T}{d \ln P} \right)_* \right], \qquad (7)$$

where $g = GM/R^2 = 1.87 \times 10^{14}$ cm s^{-2} $M_{1.4} R_6^{-2}$ is the surface gravitational acceleration (ignoring the effects of general relativity), $\chi_Q = \partial \ln P/\partial \ln Q$, with all other intensive variables set constant, $\nabla_{\rm ad} = (\partial \ln T/\partial \ln P)_{\rm ad}$ is the adiabatic temperature gradient, the asterisk refers to derivatives of the envelope's profile, and the pressure scale height is

$$H = P/\rho g = 33.1 \text{ cm } \mu_{1.33}^{-1} T_8, \qquad (8)$$

where $T_8 \equiv T/(10^8 \text{ K})$. For these analytic estimates we assume an ideal gas equation of state and use a pure helium composition with a mean molecular weight of $\mu = 1.33\mu_{1.33}$. We omit the scalings with mass and radius to simplify presentation. The compositional buoyancy is (Bildsten & Cumming 1998)

$$N_\mu^2 = -\frac{g}{H\chi_\rho} \left[\chi_{\mu_e} \left(\frac{d \ln \mu_e}{d \ln P} \right)_* + \chi_{\mu_i} \left(\frac{d \ln \mu_i}{d \ln P} \right)_* \right], \quad (9)$$

where μ_e (μ_i) is the mean molecular weight per electron (ion). Linear analysis shows that Kelvin-Helmholtz instability occurs when Ri $< \frac{1}{4}$, which develops into strong turbulence that readily transports angular momentum. This result assumes that thermal diffusion can be ignored for the unstable fluid perturbations, in other words, that the perturbations are adiabatic.

Fluid perturbations with a characteristic size L and speed V become nonadiabatic when the timescale for thermal diffusion, L^2/K, where K is the thermal diffusivity, is less than the timescale of the perturbation, L/V. The ratio of these two timescales is the Péclet number, Pe $\equiv VL/K$ (Townsend 1958). The restoring force provided by thermal buoyancy is weakened when Pe < 1, which requires the substitution of $N_T^2 \rightarrow \text{Pe}N_T^2$ and promotes instability for regions where $N_T > N_\mu$. Thermal diffusion is most efficient at small length scales, which motivates setting $LV/\nu_k = \text{Re}_c$ (Zahn 1992), where ν_k is the kinematic viscosity and Re$_c$ is the critical Reynolds number for turbulence, which is of order 1000. This gives the Péclet number approximately related to the Prandtl number, Pr, by Pe $\approx \text{Re}_c$ Pr. The turbulent perturbations are thus nonadiabatic when (Zahn 1992)

$$K > \nu_k \text{Re}_c. \qquad (10)$$

In the nondegenerate surface layers, the kinematic viscosity is dominated by ions and has a value of (Spitzer 1962)

$$\nu_k = 1.4 \times 10^{-3} \text{ cm}^2 \text{ s}^{-1} \rho_6^{-1} T_8^{5/2}, \qquad (11)$$

where $\rho_6 \equiv \rho/(10^6 \text{ g cm}^{-3})$ and we assume a Coulomb logarithm of $\ln \Lambda = 20$. Setting $K = 16\sigma_{\rm SB} T^3/(3c_p\kappa\rho^2)$, where $\sigma_{\rm SB}$ is the Stefan-Boltzmann constant, c_p is the specific heat, and κ is the opacity, the thermal diffusivity is

$$K = 48.8 \text{ cm}^2 \text{ s}^{-1} \mu_{1.33} \kappa_{0.04}^{-1} \rho_6^{-2} T_8^3, \qquad (12)$$

where we approximate $c_p = 5k_{\rm B}/(2\mu m_p)$ and scale the opacity to $\kappa_{0.04} \equiv \kappa/(0.04 \text{ cm}^2 \text{ g}^{-1})$ (the opacity is largely given by electron scattering, but is decreased by degeneracy effects; see Paczyński 1983; Bildsten 1998a). Substituting equations (11) and (12) into equation (10), we find that the perturbations are nonadiabatic

at depths of $\rho \lesssim 3 \times 10^7$ g cm^{-3} $T_8^{1/2}$. The new "secular" Richardson number associated with this limit is

$$\text{Ri}_s \equiv \frac{\nu_k \text{Re}_c}{K} \frac{N_T^2}{q^2\Omega^2}. \qquad (13)$$

When Ri$_s < \frac{1}{4}$, the so-called secular shear instability arises.

The competing effects of accretion increasing q versus turbulence developing when Ri$_s < \frac{1}{4}$ (and decreasing q) drive the surface layers toward marginally satisfying Ri$_s = \frac{1}{4}$ (assuming at this moment that the sole viscous mechanism is the Kelvin-Helmholtz instability). This expectation is borne out in the white dwarf studies of Yoon & Langer (2004). Thus, we can trivially estimate the q due to this mechanism. The thermal buoyancy is (Bildsten 1998a)

$$N_T = \left(\frac{3}{20} \frac{g}{H} \right)^{1/2} = 9.2 \times 10^5 \text{ s}^{-1} \mu_{1.33}^{1/2} T_8^{-1/2}. \qquad (14)$$

We substitute Ri$_s = \frac{1}{4}$ into equation (13) and, assuming Re$_c = 1000$, solve for a shear rate of

$$q_{\rm KH} = 223\kappa_{0.04}^{1/2}\rho_6^{1/2}T_8^{-3/4}\Omega_{0.1}^{-1}, \qquad (15)$$

where $\Omega_{0.1} = \Omega/(0.1\Omega_K)$. A shear rate this large would promote prodigious viscous heating, as well as ample mixing, but as we soon show, such a large shear is prohibited by other instabilities.

2.2. Baroclinic Instability

Another important hydrodynamic instability that has been studied extensively for accreting degenerate stars is the baroclinic instability (Fujimoto 1993), which we quickly summarize here. The interested reader should consult Fujimoto (1987, 1988) for further details (see also the discussion in Cumming & Bildsten [2000]).

The baroclinic instability arises because surfaces of constant pressure and density no longer coincide if hydrostatic balance is to be maintained when differential rotation is present. In such a configuration, fluid perturbations along nearly horizontal directions are unstable, although with a sufficient radial component to allow mixing of angular momentum and material. The instability can roughly be broken into two limits, depending on a critical baroclinic Richardson number (Fujimoto 1987)

$$\text{Ri}_{\rm BC} \equiv 4 \left(\frac{R}{H} \right)^2 \left(\frac{\Omega}{N} \right)^2 = 8.5 \times 10^3 \mu_{1.33} T_8^{-1} \Omega_{0.1}^2. \quad (16)$$

When Ri $>$ Ri$_{\rm BC}$, Coriolis effects limit the horizontal scale of perturbations. This results in two parameterizations for viscosity estimated from linear theory (Fujimoto 1993),

$$\nu_{\rm BC} = \begin{cases} \dfrac{1}{3} \dfrac{1}{\text{Ri}^{1/2}} H^2\Omega, & \text{Ri} \leq \text{Ri}_{\rm BC}, \\[2mm] \dfrac{1}{3} \dfrac{\text{Ri}_{\rm BC}}{\text{Ri}^{3/2}} H^2\Omega, & \text{Ri} > \text{Ri}_{\rm BC}, \end{cases} \qquad (17)$$

where a factor of order unity is usually included in these prescriptions, called $\alpha_{\rm BC}$, to account for uncertainty in how linear theory relates to the saturated amplitudes of the instability. For simplicity, we set $\alpha_{\rm BC} = 1$ in our analysis below.

By substituting $\nu_{\rm BC}$ into the angular momentum equation (eq. [4]), we solve for the shearing profile. Since we are interested in how the shear relates to the bursting properties, it useful to write

these results in terms of the local accretion rate $\dot{m} = \dot{M}/(4\pi R^2)$, which is typically parameterized in terms of the local Eddington rate

$$
\begin{aligned}
\dot{m}_{\mathrm{Edd}} &= \frac{2m_p c}{(1+X)R\sigma_{\mathrm{T}}} \\
&= \frac{1.5 \times 10^5 \ \mathrm{g \ cm^{-2} \ s^{-1}}}{(1+X)R_6},
\end{aligned} \tag{18}
$$

where X is the hydrogen mass fraction and σ_{T} is the Thomson cross section. The Richardson number in each case is then

$$
\mathrm{Ri} = \begin{cases} 2.2 \times 10^3 \mu_{1.33}^{-3/2} \rho_6 T_8^{3/2} \dot{m}_{0.1}^{-1} \Omega_{0.1}, & \mathrm{Ri} \le \mathrm{Ri}_{\mathrm{BC}}, \\ 4.4 \times 10^3 \mu_{1.33}^{-1/4} \rho_6^{1/2} T_8^{1/4} \dot{m}_{0.1}^{-1/2} \Omega_{0.1}^{3/2}, & \mathrm{Ri} > \mathrm{Ri}_{\mathrm{BC}}, \end{cases} \tag{19}
$$

where $\dot{m}_{0.1} = \dot{m}/(0.1\dot{m}_{\mathrm{Edd}})$ and we have used the hydrogen-deficient ($X = 0$) value for $\dot{m}_{\mathrm{Edd}}$ (eq. [18]). The transition to the case $\mathrm{Ri} \gtrsim \mathrm{Ri}_{\mathrm{BC}}$ occurs roughly at depths $\rho \gtrsim 4 \times 10^6 \ \mathrm{g \ cm^{-3}} \ T_8^{-5/2}$. The shear rate for each case is

$$
q_{\mathrm{BC}} = \begin{cases} 14\mu_{1.33}^{5/4} \rho_6^{-1/2} T_8^{-5/4} \dot{m}_{0.1}^{1/2} \Omega_{0.1}^{-3/2}, & \mathrm{Ri} \le \mathrm{Ri}_{\mathrm{BC}}, \\ 9.9\mu_{1.33}^{5/8} \rho_6^{-1/4} T_8^{-5/8} \dot{m}_{0.1}^{1/4} \Omega_{0.1}^{-7/4}, & \mathrm{Ri} > \mathrm{Ri}_{\mathrm{BC}}. \end{cases} \tag{20}
$$

This demonstrates that generally $q_{\mathrm{BC}} \ll q_{\mathrm{KH}}$, so that the baroclinic instability triggers before the Kelvin-Helmholtz instability. This prevents the shear rate from ever becoming large enough for the Kelvin-Helmholtz instability to operate at depths of $\rho \gtrsim 6 \times 10^4 \ \mathrm{g \ cm^{-3}}$.

2.3. Other Hydrodynamic Instabilities

In addition to the two instabilities described above, there are a number of other possibilities including, but not limited to, Eddington-Sweet circulation (von Zeipel 1924a, 1924b; Baker & Kippenhahn 1959), Solberg-Høiland instability (Wasiutyński 1946; Tassoul 1978; Endal & Sofia 1978), Goldreich-Schubert-Fricke instability (Goldreich & Schubert 1967; Fricke 1968), and Ekman pumping (Pedlosky 1987). At this time we avoid assessing each of these individually. As we show below, magnetic fields are likely to dominate and are interesting since they have received the least attention in past works.

3. THE IMPORTANCE OF MAGNETIC EFFECTS

Given the larger than order unity shear rates derived above, we estimate the consequences this has for a magnetic field. The point we want to emphasize is that even a reasonably small field will be wrapped by the shear flow until it becomes dynamically important.

Assuming shellular rotation, a component of radial field is stretched to have a toroidal component, $B_\phi = nB_r$, where n is the number of differential turns, given as $n = q\Omega t$, and t is the duration of the shearing. The toroidal field growth is very fast. For the Kelvin-Helmholtz case, $B_\phi \sim B_r$ in merely $\sim 10^{-6}$ s ($\sim 10^{-4}$ s for the baroclinic case). As the toroidal field becomes larger, it exerts an azimuthal stress on the shearing layer equal to $B_r B_\phi/(4\pi)$, which can be written as an effective viscosity, ν_e,

$$
B_r B_\phi/(4\pi) = \rho\nu_e q\Omega. \tag{21}
$$

In a timescale $t \approx H_\Omega^2/\nu_e$, this torquing significantly decreases the spin of the layer, where $H_\Omega = dz/d\ln\Omega = R/q$ is the shearing

scale height. Setting $B_\phi = q\Omega t B_r$, we solve for the critical initial radial field needed to affect the shearing,

$$
B_{r,\mathrm{crit}} = (4\pi\rho)^{1/2} \frac{H_\Omega}{t} = (4\pi\rho)^{1/2} \frac{R}{qt}, \tag{22}
$$

so that t is basically the Alfvén travel time through a shearing scale height. Using $\rho \approx 10^6 \ \mathrm{g \ cm^{-3}}$ as the burning density and $t \approx 1$ hr, a fiducial timescale for accumulation, our estimates for q_{KH} and q_{BC} imply $B_{r,\mathrm{crit}} \sim 10^4$ and $\sim 10^5$ G, respectively. Any initial field larger than this gets so wound up that Lorentz forces alter the shearing profile.

It is possible that the intrinsic magnetic field of the NS may be large enough that magnetic stresses never allow the shear rates to become so large. Spruit (1999) argued that this depends on the "rotational smoothing time," the timescale for nonaxisymmetric components of the magnetic field to be expelled as differential rotational brings field with opposite polarities together. This timescale is estimated as

$$
t_\Omega = \left(\frac{3R^2\pi^2}{\eta\Omega^2 q^2}\right)^{1/3}, \tag{23}
$$

where η is the magnetic diffusivity, which in the nondegenerate limit is given by (Spitzer 1962)

$$
\eta \approx 0.7 \ \mathrm{cm^2 \ s^{-1}} \ T_8^{-3/2}. \tag{24}
$$

If t_Ω is larger than the Alfvén travel time through the layer (given by t in eq. [22]), then there is sufficient time for magnetic torques to act and the shearing is merely a perturbation on the magnetic field that is quickly damped away. On the other hand, if t_Ω is sufficiently small, then the shear dominates and the magnetic field is made axisymmetric on a timescale t_Ω. Substituting t_Ω into equation (22), we estimate the critical field below which shear dominates,

$$
\begin{aligned}
B_\Omega &= (4\pi\rho)^{1/2} \left(\frac{\eta\Omega^2 R}{3\pi^2}\right)^{1/3} q^{-1/3} \\
&= 1.3 \times 10^7 \ \mathrm{G} \ \rho_6^{1/2} T_8^{-1/2} \Omega_{0.1}^{2/3} q^{-1/3}. \tag{25}
\end{aligned}
$$

The lack of persistent pulsations from accreting NSs implies a dipole field strength $\lesssim 5 \times 10^7$ G (Piro & Bildsten 2005). We therefore consider it plausible that they may have intrinsic magnetic fields $< B_\Omega$. In this case, we expect a very axisymmetric magnetic field to be created in a timescale of $t_\Omega \sim 200$ s, which is then wrapped until it becomes dynamically important.

3.1. The Tayler-Spruit Dynamo

As the toroidal magnetic field continues to wrap, it becomes increasingly important to the dynamics of the shearing and is also subject to magnetohydrodynamic instabilities. The combination of these effects has been shown to give rise to the Tayler-Spruit dynamo (Spruit 2002). In this picture, shearing grows the toroidal field, which then initiates Tayler instabilities (nonaxisymmetric, pinchlike instabilities including stratification; Tayler 1973; Spruit 1999). This turbulently creates poloidal field components that once again shear to be toroidal. This cycle continues, creating a steady state field.

The minimum shear needed for this process to operate can be argued simply. (See Spruit [2006] for a mathematical derivation that uses the dispersion relation from Acheson [1978].) We note

that Denissenkov & Pinsonneault (2007) have recently given an alternate prescription for this same mechanism using solely heuristic arguments. Since their results have not been shown consistent with a more rigorous mathematical analysis, we consider Spruit's conclusions more reliable at this time. A vertical perturbation, l_z, is limited by buoyancy forces to be (eq. [6] from Spruit 2002)

$$l_z < R\omega_A/N, \qquad (26)$$

where $\omega_A = B/[(4\pi\rho)^{1/2}R]$ is the Alfvén frequency. At small length scales, magnetic diffusion damps out perturbations. In the limit of $\Omega \gg \omega_A$, which we are considering, the Tayler instability growth rate is $\sigma_B = \omega_A^2/\Omega$, so that

$$l_z^2 > \eta/\sigma_B = \eta\Omega/\omega_A^2. \qquad (27)$$

Combining these two relations gives the minimum ω_A needed for the dynamo to act,

$$\left(\frac{\omega_A}{\Omega}\right)^4 > \frac{\eta}{R^2\Omega}\left(\frac{N}{\Omega}\right)^2. \qquad (28)$$

During the timescale for Tayler instability, σ_B^{-1}, B_r is stretched into B_ϕ by an amount

$$B_\phi = \sigma_B^{-1}q\Omega B_r. \qquad (29)$$

The largest amplification is achieved for magnetic fields that extend the largest radial length scale available, so that assuming equation (26) is marginally satisfied along with the induction equation, we find $B_r/B_\phi = l_z/R = \omega_A/N$. Combining this with equation (29), we obtain $q = (N/\Omega)(\omega_A/\Omega)$. Substituting this into equation (28), we find (Spruit 2002)

$$q_{\min} = \left(\frac{N}{\Omega}\right)^{7/4}\left(\frac{\eta}{R^2N}\right)^{1/4} \qquad (30)$$

as the minimum shear needed for the Tayler instability to operate. Although this result is consistent with more rigorous analysis (Spruit 2006), it should be viewed with some caution as we apply it to accreting NSs. The thin shell geometry we consider is quite different from the spherical geometries typically used when invoking the Tayler-Spruit dynamo. Simulations by Braithwaite (2006) demonstrate that the Tayler instability is strongest along the rotation axis, which is only realized at the poles in the NS case. Since we find the dynamo to be so much stronger than any hydrodynamic transport mechanisms, we consider it to be a reasonable approximation for these magnetic effects, even if its strength is decreased due to geometry.

The value of N used to evaluate equation (30) depends on what is supplying the buoyancy. We follow Spruit (2002) and separately consider cases of $N_\mu \gg N_T$ and $N_\mu \ll N_T$, denoted as case 0 and 1, respectively. In case 1, nonadiabatic effects become important when $\eta/K < 1$, and we must take $N_T^2 \rightarrow (\eta/K)N_T^2$ (analogous to the above analysis of the secular shear instability). For this case, which dominates for most of the envelope, we find

$$q_{\min} = 0.10\kappa_{0.04}^{3/4}\rho_6^{3/2}T_8^{-9/2}\Omega_{0.1}^{-7/4}. \qquad (31)$$

Both q_{KH} and q_{BC} are considerably above this; thus, the Tayler-Spruit dynamo activates long before the onset of purely hydrodynamic instabilities.

By assuming that equation (28) is marginally satisfied, Spruit (2002) derived the steady state field strengths. We summarize the relevant prescriptions needed for our study. The steady state azimuthal and radial field components are

$$B_{\phi0} = (4\pi\rho)^{1/2}Rq\Omega^2/N_\mu, \qquad (32)$$

$$B_{r0} = q\left(\Omega/N_\mu\right)^2 B_{\phi0}, \qquad (33)$$

for case 0. For case 1,

$$B_{\phi1} = (4\pi\rho)^{1/2}R\Omega q^{1/2}\left(\frac{\Omega}{N_T}\right)^{1/8}\left(\frac{K}{R^2N_T}\right)^{1/8}, \qquad (34)$$

$$B_{r1} = \left(\frac{\Omega}{N_T}\right)^{1/4}\left(\frac{K}{R^2N_T}\right)^{1/4}B_{\phi1}. \qquad (35)$$

The effective viscosities, as defined by equation (21), are

$$\nu_0 = R^2\Omega q^2\left(\frac{\Omega}{N_\mu}\right)^4, \qquad (36)$$

$$\nu_1 = R^2\Omega\left(\frac{\Omega}{N_T}\right)^{1/2}\left(\frac{K}{R^2N_T}\right)^{1/2}. \qquad (37)$$

Although these viscosities are appropriate for angular momentum transport, mixing of material is less efficient, since it requires expending work to exchange fluid elements (vs. just exerting shear stresses). The mixing diffusivities are

$$D_0 = R^2\Omega q^4\left(\frac{\Omega}{N_\mu}\right)^6, \qquad (38)$$

$$D_1 = R^2\Omega q\left(\frac{\Omega}{N_T}\right)^{3/4}\left(\frac{K}{R^2N_T}\right)^{3/4}, \qquad (39)$$

which is just equal to the effective turbulent magnetic diffusivity. In the Appendix we show that these prescriptions are consistent with energy conservation considerations.

3.2. Shearing Profile

The Tayler-Spruit dynamo transports angular momentum, causes viscous heating, and mixes material. We follow the procedure we used for the baroclinic case and assume steady state angular momentum transport. This is a good approximation when the viscous timescale, $t_{\text{visc}} = H^2/\nu$, is less than the timescale of accretion. For these initial estimates we focus on the $N_T \gg N_\mu$ limit (case 1), since this dominates except at compositional boundaries (which we revisit in § 4). Substituting ν_1 into equation (4), the shear rate for the Tayler-Spruit dynamo is

$$q_{TS} = \frac{\dot{m}}{R\rho\Omega}\frac{\Omega_K}{\Omega}\left(\frac{N}{\Omega}\right)^{1/2}\left(\frac{R^2N}{K}\right)^{1/2}. \qquad (40)$$

Scaling to values appropriate for accreting NSs,

$$q_{TS} = 0.38\kappa_{0.04}^{1/2}T_8^{-2}\dot{m}_{0.1}\Omega_{0.1}^{-5/2}. \qquad (41)$$

Note the scalings with $\dot{m}$ and Ω. At high $\dot{m}$, angular momentum is fed into the star faster, creating more shear. At low Ω, the shear is greater because of the larger relative angular speed between the accreted material and the NS. These are generic features we expect for any viscous mechanism (compare the scaling of q_{TS} with q_{KH} and q_{BC} from eqs. [15] and [20], respectively). The viscosity that

gives the smallest shear rate will likely be the most important at a given depth. Using this criterion, we find that the Tayler-Spruit dynamo is dominant for densities $\rho \gtrsim 3$ g cm^{-3} $T_8^{-5/2}\dot{m}_{0.1}^2\Omega_{0.1}^{-3}$, or $\rho \gtrsim 5 \times 10^3$ g cm^{-3} for $T \approx 5 \times 10^6$ K. At shallower depths, Kelvin-Helmholtz instabilities damp the shear, which is consistent with the use of hydrodynamic instabilities by Inogamov & Sunyaev (1999) for understanding the initial spreading of accreted material in the boundary layer.

The steady state magnetic field components are

$$B_\phi = 1.3 \times 10^{10} \text{ G } \kappa_{0.04}^{-1/8}\rho_6^{1/4}T_8^{-1/2}\dot{m}_{0.1}^{1/2}\Omega_{0.1}^{-1/8}, \quad (42)$$

$$B_r = 2.1 \times 10^5 \text{ G } \kappa_{0.04}^{-3/8}\rho_6^{-1/4}T_8^{1/2}\dot{m}_{0.1}^{1/2}\Omega_{0.1}^{1/8}. \quad (43)$$

Cumming & Bildsten (2000) argue that if $B_r \gtrsim 10^6$ G, it would become dynamically important to determining the drift of X-ray burst oscillations (Muno et al. 2002). The interaction of such fields with the shearing of an X-ray burst from an accreting millisecond pulsar has been explored by Lovelace et al. (2007). At high accretion rates, B_r increases and comes close to this limit, suggesting that these magnetic fields may be important for understanding the dynamics of X-ray burst oscillations, even from NSs that do not show persistent pulsations (which are preferentially seen at high accretion rates; Muno et al. 2004).

3.3. *Viscous Heating*

Viscous shearing heats the surface layer, which can also be thought of as the rate of magnetic energy destruction as the dynamo builds and destroys magnetic field (Maeder & Meynet 2004). The heating rate per unit mass is

$$\epsilon = (1/2)\nu(q\Omega)^2, \quad (44)$$

which for the Tayler-Spruit dynamo becomes

$$\epsilon_{TS} = 5.6 \times 10^{10} \text{ ergs g}^{-1}\text{ s}^{-1} \kappa_{0.04}^{1/2}\rho_6^{-1}T_8^{-2}\dot{m}_{0.1}^2\Omega_{0.1}^{-3/2}. \quad (45)$$

To put this number into perspective, we express it in terms of the energy released per accreted nucleon. This is found by multiplying the above result by the total mass per unit area down to the depth of interest, $y \approx H\rho$ (the column depth), and dividing by $\dot{m}$. We then find

$$\frac{dE_{TS}}{d\ln y} = 0.13 \text{ keV nucleon}^{-1} \mu_{1.33}^{-1}\kappa_{0.04}^{1/2}T_8^{-1}\dot{m}_{0.1}\Omega_{0.1}^{-3/2}. \quad (46)$$

In comparison, the thermal energy at 10^8 K is ≈ 10 keV nucleon^{-1}, and the burning of helium into carbon releases ≈ 0.6 MeV nucleon^{-1}. We conclude that viscous processes do not heat the layer sufficiently to alter X-ray bursts.

3.4. *Turbulent Mixing*

It is not immediately clear how much of an observational impact is provided by the magnetic fields and viscous heating estimated above. In contrast, as we shall show, shear mixing produced by the dynamo could have important ramifications for the structure and composition of the surface layers. For this reason, we devote most of the remainder of our study to investigating the consequences of mixing.

We first consider some estimates that highlight mixing's importance. For this, we parameterize the mixing diffusivity as $\alpha_{TS}D$, where D is given by equations (38) or (39) and α_{TS} is a factor of order unity that accounts for uncertainties in the Tayler-Spruit

prescription. The features we find are general enough that other viscosities can be incorporated by increasing or decreasing α_{TS}.

The material becomes fully mixed over a scale height H in a time $t_{mix} = H^2/(\alpha_{TS}D)$, which gives for case 1 ($N_T \gg N_\mu$)

$$t_{mix} = 4.3 \times 10^2 \text{ s } \alpha_{TS}^{-1}\mu_{1.33}^{-2}\kappa_{0.04}^{1/4}\rho_6^{3/2}T_8\dot{m}_{0.1}^{-1}\Omega_{0.1}^{3/4}. \quad (47)$$

Accretion is also advecting material downward, which happens in a timescale $t_{acc} = y/\dot{m} \approx \rho H/\dot{m}$,

$$t_{acc} = 2.2 \times 10^3 \text{ s } \mu_{1.33}^{-1}\rho_6 T_8\dot{m}_{0.1}^{-1}. \quad (48)$$

The ratio of these timescales is

$$t_{mix}/t_{acc} = 0.19\alpha_{TS}^{-1}\mu_{1.33}^{-1}\kappa_{0.04}^{1/4}\rho_6^{1/2}\Omega_{0.1}^{3/4}. \quad (49)$$

The scaling with ρ shows that mixing is generally more important than advection at shallow depths ($\rho \lesssim 3 \times 10^7$ g cm^{-3}), while the scaling with Ω shows that mixing is more important for slower spinning NSs (as expected from our discussion of shear rates in § 3.2).

4. ACCUMULATING, NONMIXED MODELS

We now use numerical calculations to consider the angular momentum transport through the surface layers. In this section we calculate accumulating models without directly incorporating the effects from mixing. This verifies many of the analytic estimates derived above and motivates when mixing must be included (which is done for models in § 5).

4.1. *Shear Profile Calculations*

We calculate the envelope profile for helium accumulating on an iron ocean (which represents the iron-peak ashes from previous X-ray bursts). As discussed in § 2.2, we approximate the surface as having a constant gravitational acceleration and plane-parallel geometry. In addition to using z as our radial coordinate, we find it useful to use the column depth y, defined as $dy = -\rho \, dz$, giving a pressure $P = gy$ from hydrostatic balance. We solve for ρ using the analytic equation of state from Paczyński (1983). For the liquid phase, when $1 \leq \Gamma \leq 173$, where $\Gamma = (4\pi n_i/3)^{1/3}Z^2e^2/(k_BT)$, Z is the charge per ion, and n_i is the ion density, we include the ionic free energy of Chabrier & Potekhin (1998).

During the accumulating phase, a negligible amount of helium burning takes place, so we assume that the flux is constant and set by heating from the crust. Previous studies of accreting NSs have shown that the interior thermal balance is set by electron captures, neutron emissions, and pycnonuclear reaction in the inner crust (Miralda-Escudé et al. 1990; Zdunik et al. 1992; Bildsten & Brown 1997; Brown & Bildsten 1998; Brown 2000, 2004), which release ≈ 1 MeV/$m_p \approx 10^{18}$ ergs g^{-1} (Haensel & Zdunik 1990, 2003). Depending on the accretion rate and thermal structure of the crust, this energy is either conducted into the core or released into the ocean such that for an Eddington accretion rate up to $\approx 92\%$ of the energy is lost to the core and exits as neutrinos (Brown 2000). We therefore set the heating to 150 keV nucleon^{-1}, giving a flux 2.2×10^{21} ergs cm^{-2} s^{-1} $\langle\dot{m}\rangle_{0.1}$, where $\langle\dot{m}\rangle_{0.1}$ is the time-averaged accretion rate in units of $0.1\dot{m}_{Edd}$ and the average is over timescales of order the thermal time of the crust (many years). For simplicity, we assume $\langle\dot{m}\rangle = \dot{m}$. Recent calculations by Gupta et al. (2007) suggest that heating is stronger than previously thought, but not sufficiently high enough to qualitatively change our results. We ignore the additional flux from

compressional heating because it only contributes $\sim c_p T \sim$ 10 keV nucleon^{-1} (Bildsten 1998a).

In a one-zone estimate, ignition occurs at the base of the helium layer when (Fujimoto et al. 1981)

$$\frac{d\epsilon_{3\alpha}}{dT} = \frac{d\epsilon_{\rm cool}}{dT}, \qquad (50)$$

where $\epsilon_{3\alpha}$ is the heating rate from triple-α reactions (for which we use the rate from Fushiki & Lamb [1987] for numerical calculations),

$$\epsilon_{\rm cool} = \frac{4\sigma_{\rm SB}T^4}{3\kappa y^2}, \qquad (51)$$

and the derivatives are both taken at constant pressure. We consider models where the column of accreted helium $y_{\rm acc}$ is just at this ignition point. This allows the maximum amount of time for angular momentum redistribution during the accumulating phase. The He/Fe boundary is assumed sharp, since the timescale for diffusion between the layers is much longer than the timescale of accumulation (Brown et al. 2002).

We solve for the temperature profile by integrating the radiative diffusion equation,

$$F = \frac{16\sigma_{\rm SB}T^3}{3\kappa}\frac{dT}{dy}. \qquad (52)$$

The opacity is set using electron-scattering (Paczyński 1983), free-free, and conductive opacities (Schatz et al. 1999). There is a sharp change in opacity at the He/Fe boundary (because the high Z of the iron makes it more opaque), which means that the top of the iron layer is convectively unstable. The characteristic convective velocity estimated from $F \approx \rho V_{\rm conv}^3$ is $V_{\rm conv} \sim 10^5$ cm s^{-1}, which is much less than the local sound speed of $\sim 10^8$ cm s^{-1}. This means that the convection is very efficient, and we therefore simply set $(d\ln T/d\ln P)_* = \nabla_{\rm ad}$ in the convective region. This convective region has not been noted in previous studies, although a superadiabatic temperature gradient is apparent in figures shown in both Brown et al. (2002) and Cumming (2003). It is not yet clear how this impacts the bursting properties of NSs, and we delay exploring this in detail for a future study. Nevertheless, we must include convection so as to have accurate differentially rotating profiles.

In Figure 2 we plot the temperature profile, K and η, and N for three accumulating models. The magnetic diffusivity is set using the conductivity from Schatz et al. (1999). The base of the accumulating helium is set where unstable helium ignition occurs, as designated by the thick long-dashed line in the top panel of Figure 2 (eq. [50]). The convective zone begins just below this and is bracketed by circles at its top and bottom. The convective zone is also seen in the plot of N, since N_T is effectively zero in this region. The change in composition at the He/Fe boundary gives a large buoyancy contribution, which we estimate as

$$N_\mu \approx \left(\frac{g}{H}\Delta\ln\mu\right)^{1/2}, \qquad (53)$$

where $\Delta\ln\mu \approx 0.44$ is the logarithmic change in the mean molecular weight at the boundary. We denote this by a square for each model in the bottom panel of Figure 2. For the majority of the profile, the Tayler-Spruit dynamo is given by case 1 ($N_T \gg N_\mu$). Since $K \gg \eta$, the perturbations creating the dynamo are nonadiabatic for case 1, as we described in § 3.1. The only place case 0 ($N_\mu \gg N_T$) is important is at the He/Fe boundary.
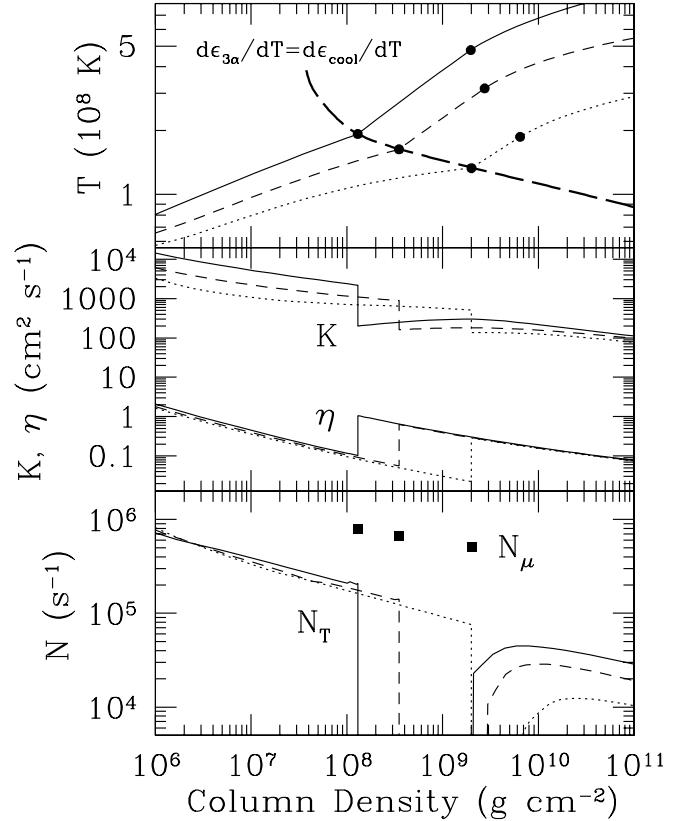

FIG. 2.—Accumulating models for accretion rates of $0.1\dot{m}_{\rm Edd}$ (*dotted lines*), $0.3\dot{m}_{\rm Edd}$ (*short-dashed lines*), and $1.0\dot{m}_{\rm Edd}$ (*solid lines*). For each model the base of the helium layer is taken to be at the unstable triple-α ignition depth, where $d\epsilon_{3\alpha}/dT = d\epsilon_{\rm cool}/dT$ (*thick long-dashed line in top panel*). The top panel plots the temperature, and the circles mark the top and bottom of the convective zone. The middle panel plots the thermal diffusivity K and magnetic diffusivity η. The bottom panel shows the Brunt-Väisälä frequency N for both thermal (N_T, *lines*) and compositional (N_μ, *squares*) contributions.

We next solve for the shear rates by solving equation (4) with either ν_0 or ν_1, depending on which case is appropriate. We assume angular momentum transport does not affect the thermal or compositional structure, in other words, that the transport is just happening "in the background." This allows us to assess which effects are crucial for subsequent iterations that include angular momentum transport in the actual structure calculation.

In Figure 3 lines denote the profiles calculated assuming case 1 of the Tayler-Spruit dynamo. We assume that the convection is effectively instantaneous in transporting material and angular momentum; thus, all the quantities become very small in the convective region. This is appropriate since the convective overturn timescale, $H/V_{\rm conv} \sim 10^{-4}$ s, is much less than the timescales for mixing or accretion. The squares indicate the corresponding values due to the compositional discontinuity found by using case 0. Since the viscous timescale, $t_{\rm visc} = H^2/\nu$, is much less than the timescale it took to accrete to this base column $t_{\rm acc} = y_{\rm acc}/\dot{m} \sim 10^3$–$10^5$ s (for the range of $\dot{m}$ considered), our steady state assumption is valid.

These calculations highlight the importance of the compositional jump, since $t_{\rm visc}$, q, and $dE/d\ln y$ are all amplified here. This is because the large buoyancy reduces angular momentum transport across this boundary. The viscous time is nearly independent of accretion rate in regions where $N_T \gg N_\mu$, because the viscosity in case 1 is independent of q. The energy deposition is always much smaller than the heat coming from the crust, and it falls off somewhat faster with depth than expected from the
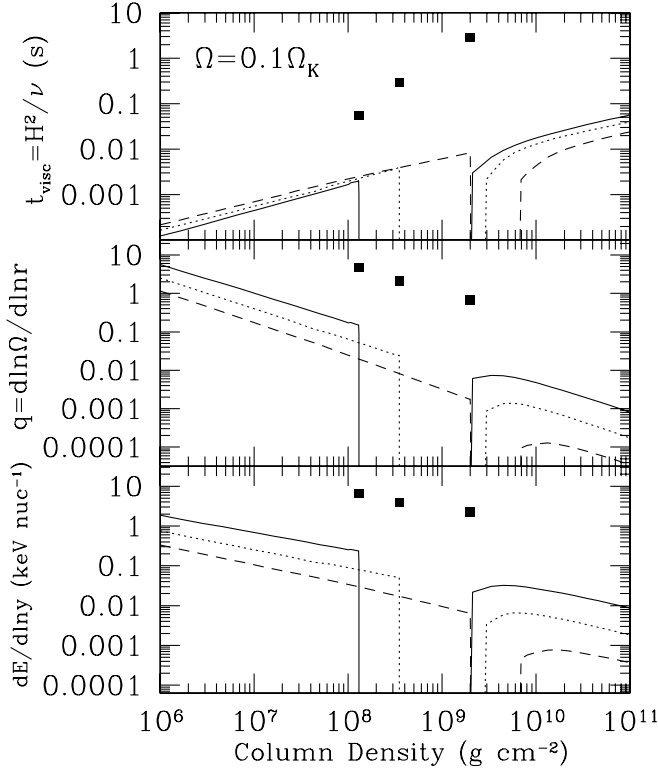
FIG. 3.—Angular momentum transport in the NS surface layers, for a spin of $\Omega = 0.1\Omega_K$ and accretion rates of $0.1\dot{m}_{Edd}$ (*dotted lines*), $0.3\dot{m}_{Edd}$ (*dashed lines*), and $1.0\dot{m}_{Edd}$ (*solid lines*). The panels display (from top to bottom) the viscous timescale for angular momentum transport across a scale height, t_{visc}, the shear rate q, and the viscous energy deposition per logarithm column, $dE/d \ln y$. The squares indicate the corresponding values due to the compositional discontinuity at the base of the accumulating layer.

estimate presented in § 3.3 due to electron degeneracy effects decreasing N_T. New heat sources at a depth of $\approx 10^{12}$ g cm^{-2} could ease the difficulty calculations have in recreating the low ignition columns needed to explain superburst recurrence times (Cumming et al. 2006), but this viscous heating is not nearly enough to correct this problem.
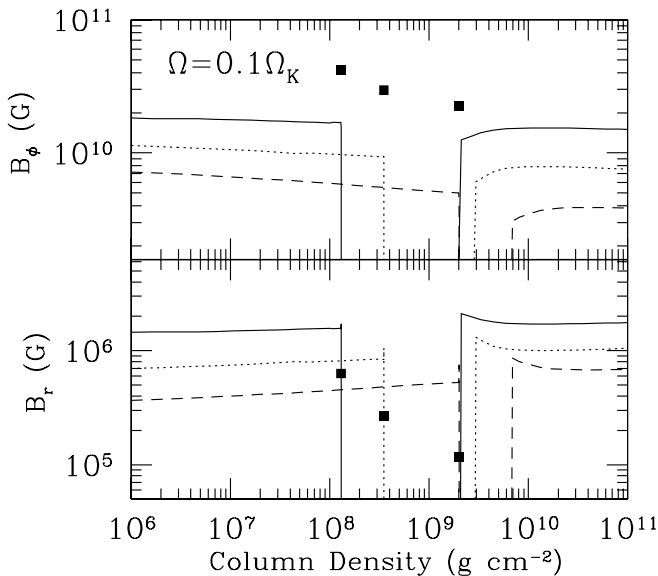

FIG. 4.—Azimuthal and radial field components for a spin of $\Omega = 0.1\Omega_K$. Lines have the same meaning as in Fig. 3.
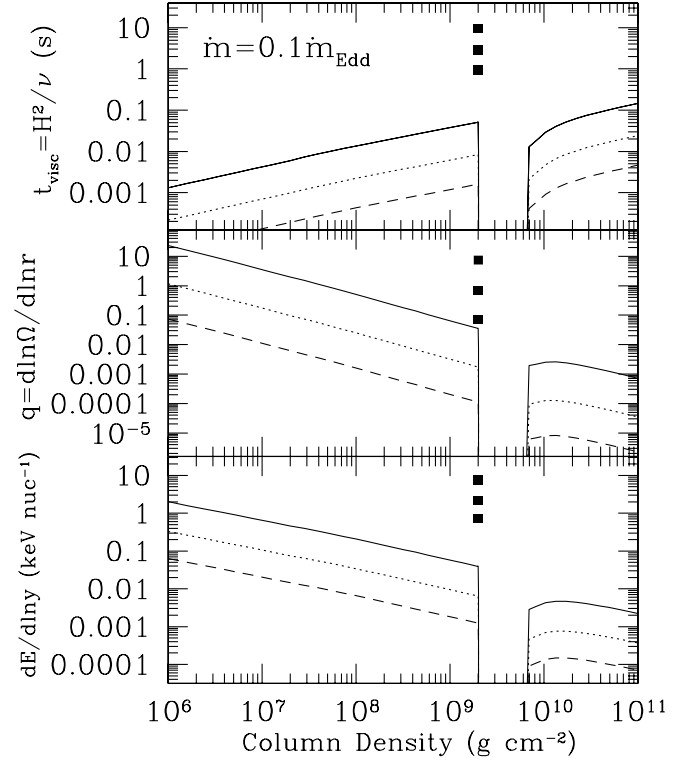

FIG. 5.—Same as Fig. 3, but for spins of $0.03\Omega_K$ (*solid lines*), $0.1\Omega_K$ (*dotted lines*), and $0.3\Omega_K$ (*dashed lines*), all for $\dot{m} = 0.1\dot{m}_{Edd}$.

In Figure 4 we plot the magnetic fields found within the radiative zones for the models from Figure 3. We assume that within the convective zone the dynamo is not able to operate, and do not calculate a magnetic field here. It is also interesting to compare these fields to those derived by Cumming et al. (2001), who calculated the steady state fields expected when Ohmic diffusion balances advection through accretion. Their principal result was that the steady state horizontal field drops by $\approx \dot{m}/0.02\dot{m}_{Edd}$ orders of magnitude from the crust up through the ocean. In contrast, the magnetic fields we find are nearly constant with depth. We therefore do not expect these fields to persist if the accretion ceases for a time and instead to be expelled on an ohmic diffusion time (~days near the top of the ocean). When the dynamo is active, the steady state is reached quickly enough that ohmic diffusion can be ignored.

In Figure 5 we compare what happens as the spin is changed by plotting $\Omega = 0.03\Omega_K$, $0.1\Omega_K$, and $0.3\Omega_K$ (67, 220, and 670 Hz, respectively), all for $\dot{m} = 0.1\dot{m}_{Edd}$. Note that the shearing is most dramatic at smaller Ω. In fact, the shearing and heating profiles are very sensitive to the value of Ω, as was demonstrated by the analytic estimates. We do not plot the associated magnetic field for these models, since we have already plotted some examples in Figure 4 and the analysis of § 3.2 provides adequate estimates.

These plots of q show that very little shearing is present. To emphasize this fact, in Figure 6 we plot the actual spin frequency as a function of depth found by integrating q for a range of accretion rates. The discontinuity at the He/Fe boundary complicates this estimate. Noting that

$$\Omega = \int q\Omega \, d \ln r = -\int q\Omega \frac{H}{R} \, d \ln y, \qquad (54)$$

we approximate the spin change at this boundary as

$$\Delta\Omega \approx q\Omega H/R. \qquad (55)$$

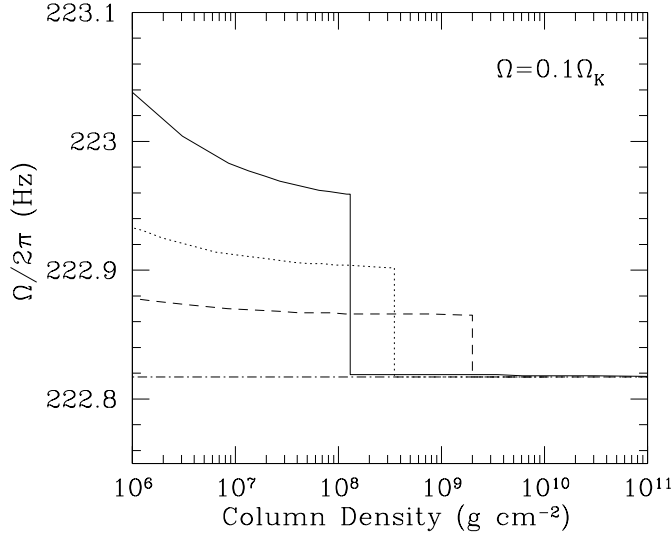FIG. 6.—Spin frequency as a function of column depth for $\Omega = 0.1\Omega_K$, with $\dot{m} = 0.1\dot{m}_{Edd}$ (dashed line), $0.3\dot{m}_{Edd}$ (dotted line), and $1.0\dot{m}_{Edd}$ (solid line). The dot-dashed line shows a constant spin frequency for comparison.

The change of spin is generally $\lesssim 0.5$ Hz across the accumulating layer, with the majority of the spin change occurring at the compositional boundary. The layer is very nearly in uniform rotation.

4.2. Mixing and the Compositional Barrier

The above calculations confirm that the viscosity is too large for either appreciable shearing or viscous heating. As demonstrated in § 3.4, mixing should be important, but Figures 3 and 5 argue that we must take into account the large N_μ at the He/Fe boundary. Assuming that N_μ scales like equation (53), we estimate

$$N_\mu = 1.6 \times 10^6 \text{ s}^{-1} \, \mu_{1.33}^{1/2} T_8^{-1/2} (\Delta \ln \mu / 0.44)^{1/2}. \quad (56)$$

We substitute this into ν_0 to solve for q using equation (4), which is used to estimate a mixing timescale at the boundary,

$$t_{mix} = H^2/(\alpha_{TS} D_0)$$
$$= 1.7 \times 10^3 \text{ s } \alpha_{TS}^{-1} \mu_{1.33}^{-5/3} \rho_6^{4/3} T_8^{5/3} \dot{m}_{0.1}^{-4/3} \Omega_{0.1} \left(\frac{\Delta \ln \mu}{0.44} \right)^{1/3}. \quad (57)$$

Using equation (48), we find a ratio of

$$\frac{t_{mix}}{t_{acc}} \approx 0.77 \alpha_{TS}^{-1} \mu_{1.33}^{-2/3} \rho_6^{1/3} T_8^{2/3} \dot{m}_{0.1}^{-1/3} \Omega_{0.1} \left(\frac{\Delta \ln \mu}{0.44} \right)^{1/3}. \quad (58)$$

Unlike in equation (49), this new ratio depends on $\dot{m}$. This is because the viscosity in case 0 has a different dependence on q. Now as $\dot{m}$ is increased, t_{mix} decreases faster than t_{acc}. Above a critical accretion rate of

$$\dot{m}_{crit,1} = 4.6 \times 10^{-2} \dot{m}_{Edd} \alpha_{TS}^{-3} \mu_{1.33}^{-2} \rho_6 T_8^2 \Omega_{0.1}^3 \left(\frac{\Delta \ln \mu}{0.44} \right), \quad (59)$$

mixing can no longer be ignored. For densities and temperatures expected at the base of the accumulating layer, this critical accretion rate lies in the range of $0.1\dot{m}_{Edd}$–$1.0\dot{m}_{Edd}$. Note that
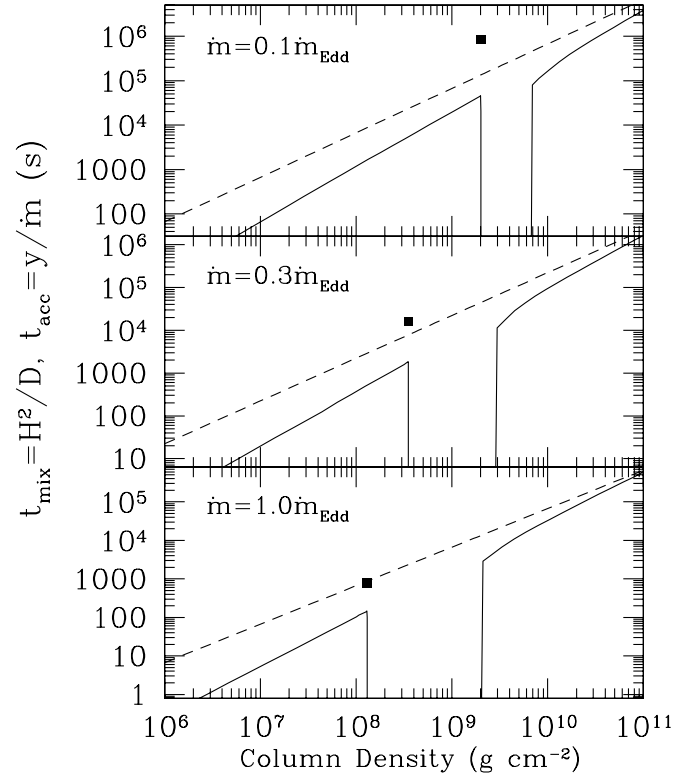

FIG. 7.—Comparison of the mixing timescale t_{mix} (solid lines) vs. the accretion timescale t_{acc} (dashed line) for $\dot{m} = 0.1\dot{m}_{Edd}$, $0.3\dot{m}_{Edd}$, and $1.0\dot{m}_{Edd}$ (top to bottom; all with $\Omega = 0.1\Omega_K$ and $\alpha_{TS} = 1$). The square denotes t_{mix} due to the compositional discontinuity. At low $\dot{m}$, the squares are above the dashed line, demonstrating that $t_{mix} > t_{acc}$ at the base of the accumulating layer, which prevents mixing to larger depths. At sufficiently high $\dot{m}$, $t_{mix} < t_{acc}$ at depths below the accumulation depth, so that mixing between helium and iron can occur.

this depends very strongly on the spin rate $\dot{m}_{crit,1} \propto \Omega^3$; thus, we expect the slower spinning NSs to be considerably more affected by mixing.

To test these analytic estimates we compare the mixing and accretion timescales in Figure 7. From the top panel to the bottom panel, we increase $\dot{m}$ (fixing $\Omega = 0.1\Omega_K$). At low $\dot{m}$, the He/Fe boundary at y_{acc} (shown by the squares) acts as a barrier to mixing, since $t_{mix} > t_{acc}$ at this depth. When this happens, it is a good approximation to ignore mixing and assume two separate layers during the accumulation phase. As $\dot{m}$ increases, t_{mix} at y_{acc} becomes less and less until finally $t_{mix} < t_{acc}$, so that material should be mixed past y_{acc}. When this occurs, our accumulating model can no longer ignore mixing. The mixing between helium and iron occurs down to a depth where t_{mix} is equal to the length of time accretion has been taking place, $t_{acc} = y_{acc}/\dot{m}$. The key point we want to emphasize is that because of the buoyancy barrier, the effect of mixing turns on abruptly, and when it does, mixing will occur well past y_{acc}.

5. THE EFFECTS OF TURBULENT MIXING

Once $t_{mix} < t_{acc}$ at the buoyancy barrier, the compositional profile of the NS is very different, which we now explore. We treat the mixing as complete, which we diagram in Figure 8 and summarize here. Material accretes at a rate $\dot{m}$ for a time t_{acc} with a helium mass fraction Y_0, supplying a column of material $y_{acc} = \dot{m}t_{acc}$. The total column of helium that accretes during this time is therefore $Y_0 y_{acc}$. Mixing causes this newly accreted material to mix past y_{acc} to the mixing depth y_{mix}, defined as where $t_{mix} = t_{acc}$.

Accretion at a rate $\dot{m}$
with He fraction Y_0
for a time t_{acc}

$y \ (g \ cm^{-2})$

Fully mixed
accumulating
material

$Y_{mix} = Y_0 y_{acc} / y_{mix}$

$y_{acc} = \dot{m} t_{acc}$

$y_{mix} = y(t_{mix} = t_{acc})$
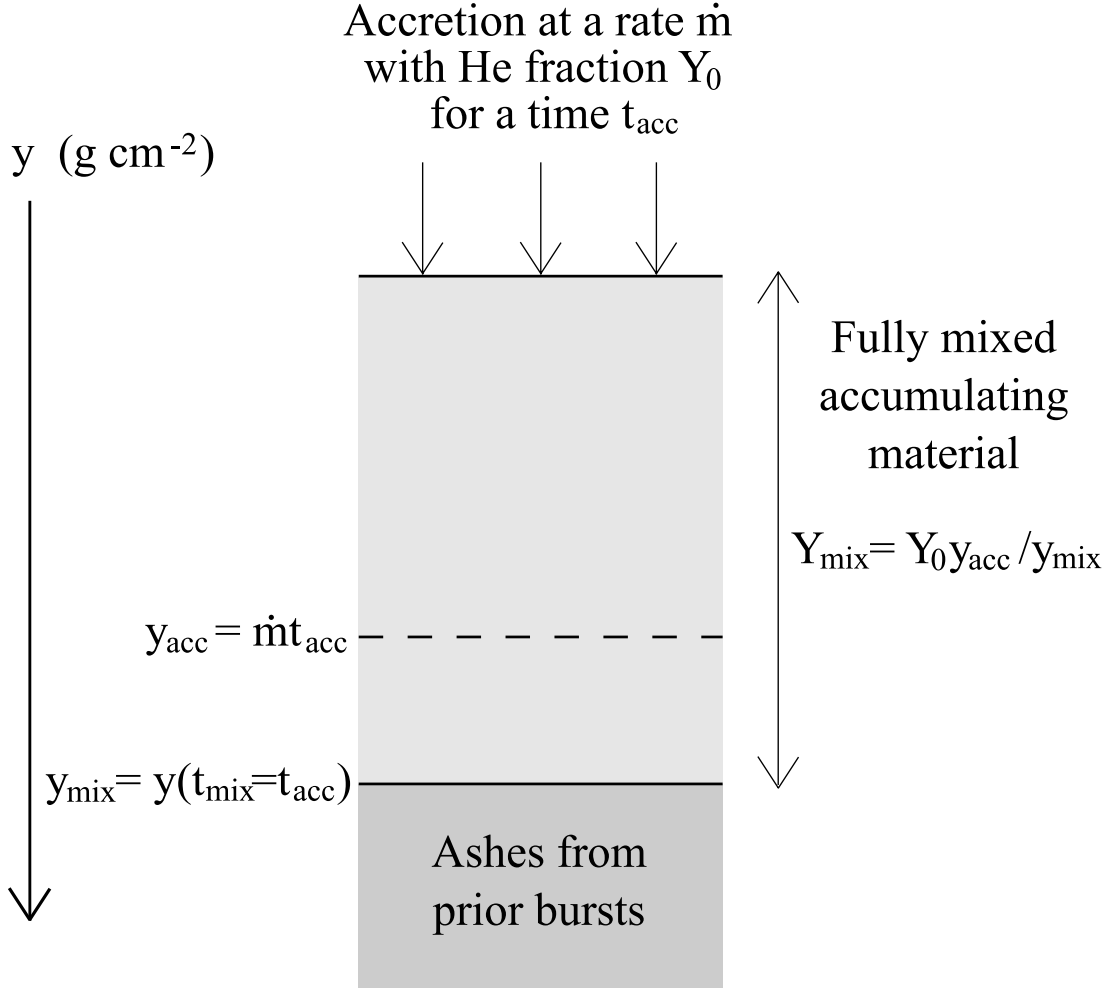
Ashes from
prior bursts

FIG. 8.—Diagram demonstrating the main features of turbulent mixing. Material mixes down to where $t_{mix} = t_{acc}$, which defines the depth y_{mix}. The total amount of material that accretes is $y_{acc} = \dot{m} t_{acc}$, giving a total accreted column of helium of $Y_0 y_{acc}$. Within the mixed layer, the helium mass fraction is diluted to a new mass fraction of $Y_{mix} = Y_0 y_{acc}/y_{mix}$.

The helium is fully mixed down to this depth, resulting in a diluted mass fraction $Y_{mix} = Y_0 y_{acc}/y_{mix}$ within the mixed layer. In the following sections we consider two scenarios that can result from the mixing: (1) unstable ignition of the mixed fuel, and (2) stable burning when the material mixes to sufficient depths.

5.1. Numerical Calculations of Mixed Ignition

As the column of accreted material grows, it can still reach the correct conditions for unstable ignition, but mixing causes two changes: (1) the ignited layer has a diluted helium fraction, $Y_{mix} < Y_0$, and (2) the ignition takes place at the base of the mixed layer, at a depth $y_{mix} > y_{acc}$, resulting in a recurrence time for ignition much less than when mixing is not included.

Both of these effects are easiest to explore using a semianalytic model. In this section all calculations use $Y_0 = 1$. We consider other values of Y_0 for our analytic estimates in § 5.2. We solve for the mixed accumulating structure by first assuming an amount of accretion y_{acc}, which for a given $\dot{m}$ implies an accretion time $y_{acc}/\dot{m}$. We integrate the radiative diffusion equation (eq. [52]) down to a depth where $t_{mix} = t_{acc}$, giving y_{mix}, where we assume a constant flux profile as was discussed in § 4, since little helium burning takes place during accumulation. We then estimate the mixed helium fraction as $Y_{mix} = y_{acc}/y_{mix}$. This estimate is improved by substituting Y_{mix} back into our envelope integration and

iterating until Y_{mix} converges. The nonhelium component in the layer is taken to be iron.

In Figure 9 we plot the resulting profiles for a NS accreting at $\dot{m} = 0.1\dot{m}_{Edd}$ and $\Omega = 0.1\Omega_K$. In the four panels we consider values of y_{acc} of 10^6, 3×10^6, 10^7, and 4×10^7 g cm^{-2} (from left to right and then top to bottom, denoted by the circles), which is meant to mimic the accumulation of fuel on the NS surface. For each integration, the envelope profile continues down to a depth y_{mix}, which also gives Y_{mix} as displayed in each panel. The last model reaches the conditions necessary for ignition at the base of the mixed layer. The recurrence time for these mixed ignition models is much less than for those without mixing. For the plotted model, the recurrence time is $t_{rec} = 4 \times 10^7$ g cm$^{-2}/(1.5 \times 10^3$ g cm^{-2} s$^{-1}) \approx 44$ minutes. In contrast, the model shown in Figure 2 with the same accretion rate of $\dot{m} = 0.1\dot{m}_{Edd}$ has $t_{rec} \approx 1.5$ days. The shorter recurrence time is not only due to mixing carrying helium down to deeper depth, but also a change in the thermal profile. Since significant iron is mixed up into the accumulating material, the free-free opacity, which scales $\kappa_{ff} \propto Z^2/A$, where Z and A are the charge and mass per nucleon, respectively, is now the dominant opacity mechanism. The accumulating layer is more opaque and therefore hotter for a given flux in comparison to the pure helium models considered before, which contributes to the shallow ignition depths.
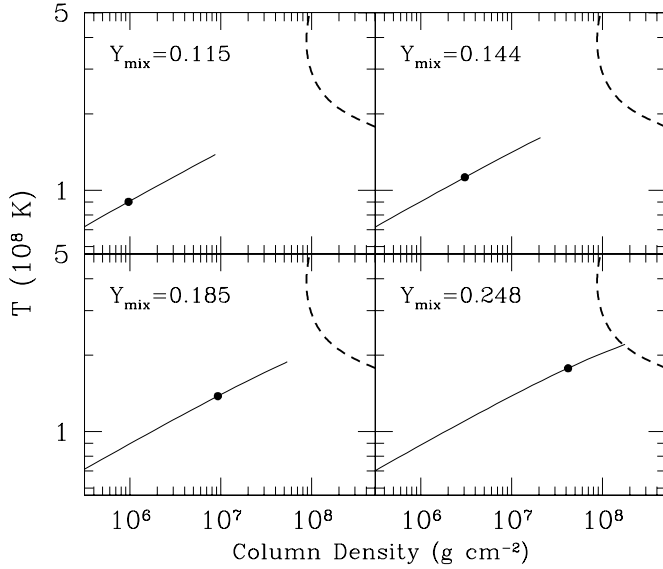
FIG. 9.—Four panels show how the fully mixed accumulating layer evolves in time until it reaches conditions necessary for unstable ignition. The parameters of the NS are $\dot{m} = 0.1\dot{m}_{Edd}$ and $\Omega = 0.1\Omega_K$. In each panel, the column of helium that has been accreted is denoted by a circle, which is from left to right and top to bottom $y_{acc} = 10^6, 3 \times 10^6, 10^7,$ and 4×10^7 g cm^{-2}. Mixing takes place down to the column reached by the thin solid line. The mixed helium fraction Y_{mix} is displayed in the upper left-hand corner of each panel. The ignition curve associated with each Y_{mix} is shown as a thick dashed line.

We calculate t_{rec} for a grid of models with various $\dot{m}$ and Ω in Figure 10. The recurrence time is shorter for stronger mixing, which occurs at high $\dot{m}$ or low Ω, and can be as short as ≈ 5–30 minutes. We warn though that all of these calculations assume that complete mixing can occur, and as we already showed in § 4, buoyancy may prevent this (eq. [59]). Nevertheless, it is interesting to calculate the mixed ignition conditions for a wide range of parameter space, because the conditions left from previous bursts may vary, and quantities such as $\Delta \ln \mu$ may be smaller at times if, for example, there is incomplete burning in a previous burst. At sufficiently high $\dot{m}$ or low Ω, the ignition takes place at
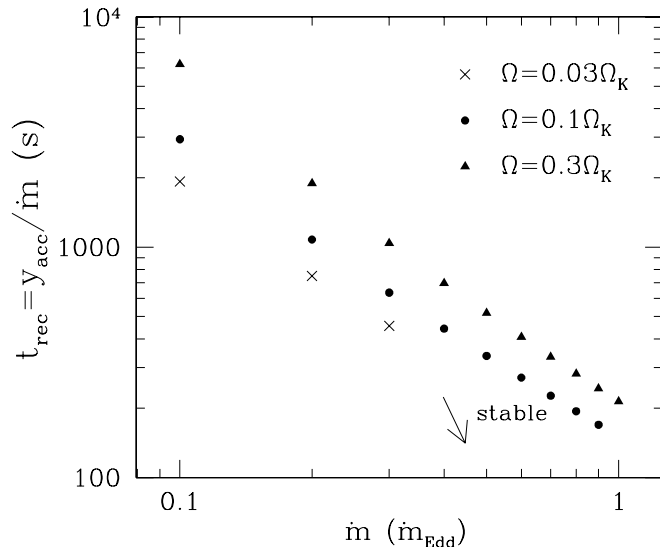

FIG. 10.—Recurrence time for mixed ignition models as a function of $\dot{m}$. The symbols denote different spins, as shown in the key. Models that are at sufficiently high $\dot{m}$ or low Ω do not ignite unstably and thus are not plotted.
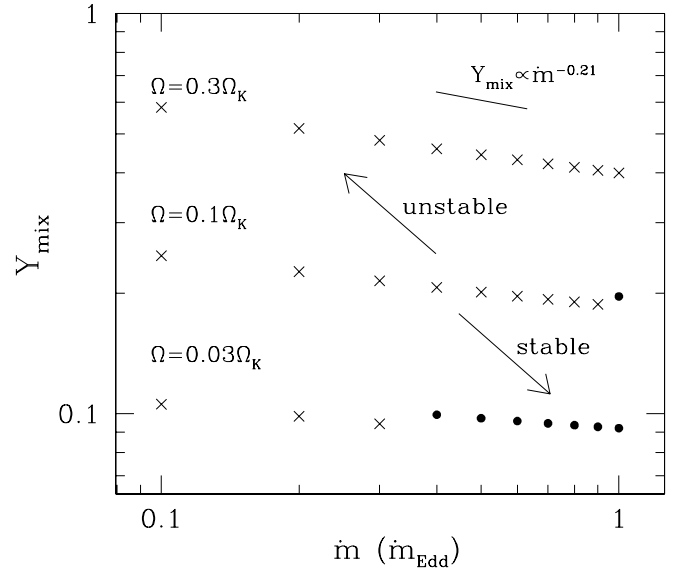

FIG. 11.—Mixed helium mass fraction Y_{mix} as a function of $\dot{m}$ and Ω. The crosses are mixed ignition models. The circles are for stably burning models and give the amount of helium present in the steady state mixing and burning layer. Steady state burning therefore requires either high $\dot{m}$ or low Ω. The scaling of $Y_{mix} \propto \dot{m}^{-0.21}$ is derived in eq. (69) and is consistent with these numerical results. Without mixing, *all of these considered models ignite unstably*, since stable accretion requires $\dot{m} \gtrsim 10\dot{m}_{Edd}$.

high enough temperatures that the envelope does not ignite unstably. We consider this case in more detail in §§ 5.3 and 5.4.

The short recurrence times that we find are similar to some seen for multiple bursts (Galloway et al. 2006 and references therein). However, our model cannot explain the energetics of these bursts. The energetics are typically quantified in a distance-independent measure, the so-called α-value, which is the ratio of energy released in the persistent emission between bursts to the energy of the burst itself. For pure helium ignition $\alpha \sim 100$. In contrast, the α-values for the short recurrence time bursts are typically ~ 10 (Boirin et al. 2007). Since the only helium that will burn in our mixed ignition models is that accreted since the last outburst, we always find $\alpha \sim 100$. Therefore, we still require an additional nuclear energy source, such as incomplete burning from the previous X-ray burst, to explain such a low α-value. This in fact may not be a problem because *incomplete burning may naturally explain the short recurrence times, since this would lead to smaller compositional gradients and therefore stronger mixing.*

We plot Y_{mix} as a function of $\dot{m}$ and Ω in Figure 11. The crosses correspond to models that ignite unstably. The circles are stable accreting models that are discussed in §§ 5.3 and 5.4. The implications of this mixed ignition for the unstable burning during the X-ray burst can be easily tested by more sophisticated numerical simulations *by just considering a mixed accumulating column*, for example, by artificially setting $Y \approx 0.1$–0.6 as shown in this Figure 11. Since viscous heating is negligible, these initial tests do not need to resolve the shearing profiles.

5.2. *Analytic Estimates of Mixed Ignition*

We now estimate the properties of the mixed ignition models. These solutions directly show how mixing depends on the properties of the accumulating layer, in particular the prefactor α_{TS} and Y_0, without having to consider a multitude of models. The effects of a free-free opacity are important in deriving the correct atmospheric conditions. To include this analytically, we use the free-free opacity from Schatz et al. (1999) simplified to a

one-component plasma and with the dimensionless Gaunt factor set to unity,

$$\kappa_{\mathrm{ff}} \approx 3.77 \ \mathrm{cm^2 \ g^{-1}} \ \frac{\rho_6}{T_8^{7/2}} \frac{Z^2}{A}, \tag{60}$$

where we have estimated $\mu_e \approx 2$ as is correct within 10% for any of the elements of interest. Integrating the radiative diffusion equation (eq. [52]), assuming a constant flux of $F = 10^{21}$ ergs cm^{-2} s^{-1} F_{21} and an ideal gas equation of state, the temperature as a function of column y is

$$T(y) = 1.8 \times 10^8 \ \mathrm{K} \ \left(\mu_{1.33} F_{21} Z^2/A\right)^{2/17} y_8^{4/17}, \tag{61}$$

where $y_8 \equiv y/10^8$ g cm^{-2}. Using equation (47), we find the mixing timescale as a function of y,

$$t_{\mathrm{mix}} = 3.5 \times 10^3 \ \mathrm{s} \ \alpha_{\mathrm{TS}}^{-1} \mu_{1.33}^{-0.44} \left(F_{21} Z^2/A\right)^{-0.19} \dot{m}_{0.1}^{-1} \Omega_{0.1}^{0.75} y_8^{1.37}. \tag{62}$$

Note that $t_{\mathrm{mix}} \propto y^{1.37}$ is a higher power than $t_{\mathrm{acc}} = y/\dot{m} \propto y$. This explicitly shows that mixing dominates at lower y, but accretion always wins at some depth. Setting t_{mix} equal to $t_{\mathrm{acc}} = y_{\mathrm{acc}}/\dot{m}$ gives the depth where mixing can extend to for a given column of accreted material y_{acc},

$$y_{\mathrm{mix}}(y_{\mathrm{acc}}) = 1.6 \times 10^8 \ \mathrm{g \ cm^{-2}} \ \alpha_{\mathrm{TS}}^{0.73} \mu_{1.33}^{0.32}$$
$$\times \left(F_{21} Z^2/A\right)^{0.14} \Omega_{0.1}^{-0.55} y_{\mathrm{acc},8}^{0.73}, \tag{63}$$

where $y_{\mathrm{acc},8} = y_{\mathrm{acc}}/(10^8$ g cm$^{-2})$. The mixed helium fraction down to this depth is

$$Y_{\mathrm{mix}}(y_{\mathrm{acc}}) = \frac{Y_0 y_{\mathrm{acc}}}{y_{\mathrm{mix}}(y_{\mathrm{acc}})}$$
$$= 0.63 \alpha_{\mathrm{TS}}^{-0.73} Y_0 \mu_{1.33}^{-0.32} \left(F_{21} Z^2/A\right)^{-0.14} \Omega_{0.1}^{0.55} y_{\mathrm{acc},8}^{0.27}. \tag{64}$$

Since $Y_{\mathrm{mix}} \propto y_{\mathrm{acc}}^{0.27}$, the strength of mixing decreases (Y_{mix} gets larger) as more material is accreted, which was demonstrated by the four panels in Figure 9.

We next estimate what ignition depth is expected for this fully mixed accumulating layer. The energy generation rate for triple-α burning is approximated as

$$\epsilon_{3\alpha} = 5.3 \times 10^{23} \ \mathrm{ergs \ g^{-1} \ s^{-1}} \ f \frac{\rho_6^2 Y_{\mathrm{mix}}^3}{T_8^3} \exp\left(-\frac{44}{T_8}\right), \tag{65}$$

where f is a factor that accounts for screening effects. To make progress analytically, we expand the exponential as $\exp(-44/T_8) \approx 7.95 \times 10^{-10}(T_8/2.1)^{21}$. Using our temperature profile (eq. [61]), the condition that $d\epsilon_{3\alpha}/dT = d\epsilon_{\mathrm{cool}}/dT$ (eq. [50]) implies an ignition depth of

$$y_{\mathrm{ign}} = 9.4 \times 10^7 \ \mathrm{g \ cm^{-2}} \ f^{-0.15} \mu_{1.33}^{-0.57}$$
$$\times F_{21}^{-0.13} \left(Z^2/A\right)^{-0.28} Y_{\mathrm{mix}}^{-0.44}. \tag{66}$$

Setting $y_{\mathrm{ign}} = y_{\mathrm{mix}}$ from equation (63), we solve for y_{acc}, the critical column of material that must be accreted to cause ignition.

This is then substituted back into equations (63) and (64) to find that ignition occurs at a depth

$$y_{\mathrm{mix,ign}} = 1.2 \times 10^8 \ \mathrm{g \ cm^{-2}} \ \alpha_{\mathrm{TS}}^{0.38} f^{-0.13} \mu_{1.33}^{-0.33}$$
$$\times Y_0^{-0.38} F_{21}^{-0.039} \left(Z^2/A\right)^{-0.17} \Omega_{0.1}^{-0.29}, \tag{67}$$

with a composition of

$$Y_{\mathrm{mix,ign}} = 0.57 \alpha_{\mathrm{TS}}^{-0.86} f^{-0.047} \mu_{1.33}^{-0.56} Y_0^{0.86}$$
$$\times F_{21}^{-0.21} \left(Z^2/A\right)^{-0.25} \Omega_{0.1}^{0.65}. \tag{68}$$

Comparing this with the numerical calculation is easiest if we assume F is set by $\dot{m}$ ($F_{21} = 2.2\dot{m}_{0.1}$) as well as scaling $Z^2/A \approx 12$ and $\mu \approx 2.1$ as appropriate for the iron-rich composition. This gives

$$Y_{\mathrm{mix,ign}} \approx 0.20 \alpha_{\mathrm{TS}}^{-0.86} \dot{m}_{0.1}^{-0.21} \Omega_{0.1}^{0.65}. \tag{69}$$

The recurrence time is $t_{\mathrm{rec}} = Y_{\mathrm{mix,ign}} y_{\mathrm{mix,ign}}/\dot{m}$, resulting in

$$t_{\mathrm{rec}} \approx 950 \ \mathrm{s} \ \alpha_{\mathrm{TS}}^{-0.48} \dot{m}_{0.1}^{-1.25} \Omega_{0.1}^{0.36}. \tag{70}$$

Equations (69) and (70) confirm the scalings found for the numerical calculations in Figures 10 and 11. We have plotted the $Y_{\mathrm{mix}} \propto \dot{m}^{-0.21}$ scaling in Figure 11 to emphasize this. These analytic results also show the dependence on the parameter α_{TS}, for which $Y_{\mathrm{mix,ign}}$ is especially sensitive.

5.3. Steady State Mixing and Burning

Another possibility is that the helium is mixed and burned by triple-α reactions in steady state, leading to stable burning. The basic idea is similar to that described above for mixed ignition, except now the depth of the accumulating layer is set by the helium burning timescale, $t_{3\alpha} = E_{3\alpha}/(Y\epsilon_{3\alpha})$, where $E_{3\alpha} = 5.84 \times 10^{17}$ ergs g^{-1} is the energy per mass released from this burning. As shown in Figure 12, material is mixed to sufficient depths where $t_{3\alpha}$ (which decreases with depth) is equal to t_{mix} (which increases with depth), which defines a mixing (or burning) depth $y_{\mathrm{mix}} = y(t_{\mathrm{mix}} = t_{3\alpha})$. During a mixing timescale, the amount of material that is accreted is $y_{\mathrm{acc}} = \dot{m} t_{\mathrm{mix}}(y_{\mathrm{mix}})$, so that the total column of helium that has been accreted is $Y_0 \dot{m} t_{\mathrm{mix}}(y_{\mathrm{mix}})$. This is diluted over a depth y_{mix}, so that the mixed helium fraction is $Y_{\mathrm{mix}} = Y_0 y_{\mathrm{acc}}/y_{\mathrm{mix}}$. This is all occurring in steady state; material moves through the mixed layer at a rate $\dot{m}$, but this layer does not move up or down in pressure (column) coordinates, as the burning is stable.

The basic results of steady state mixing and burning are best shown using a simple numerical model. The equation that describes helium continuity, including depletion by triple-α burning, becomes, in the plane-parallel limit (Fujimoto 1993),

$$\frac{dY}{dt} = \frac{1}{R^2 \rho} \frac{\partial}{\partial z} \left(R^2 \rho D \frac{\partial Y}{\partial z}\right) + \left(\frac{\partial Y}{\partial t}\right)_{3\alpha}. \tag{71}$$

We assume changes in ρ and D with depth are small in comparison to changes in Y, and following our derivation of the angular momentum equation in § 1.1, we take the steady state limit to derive

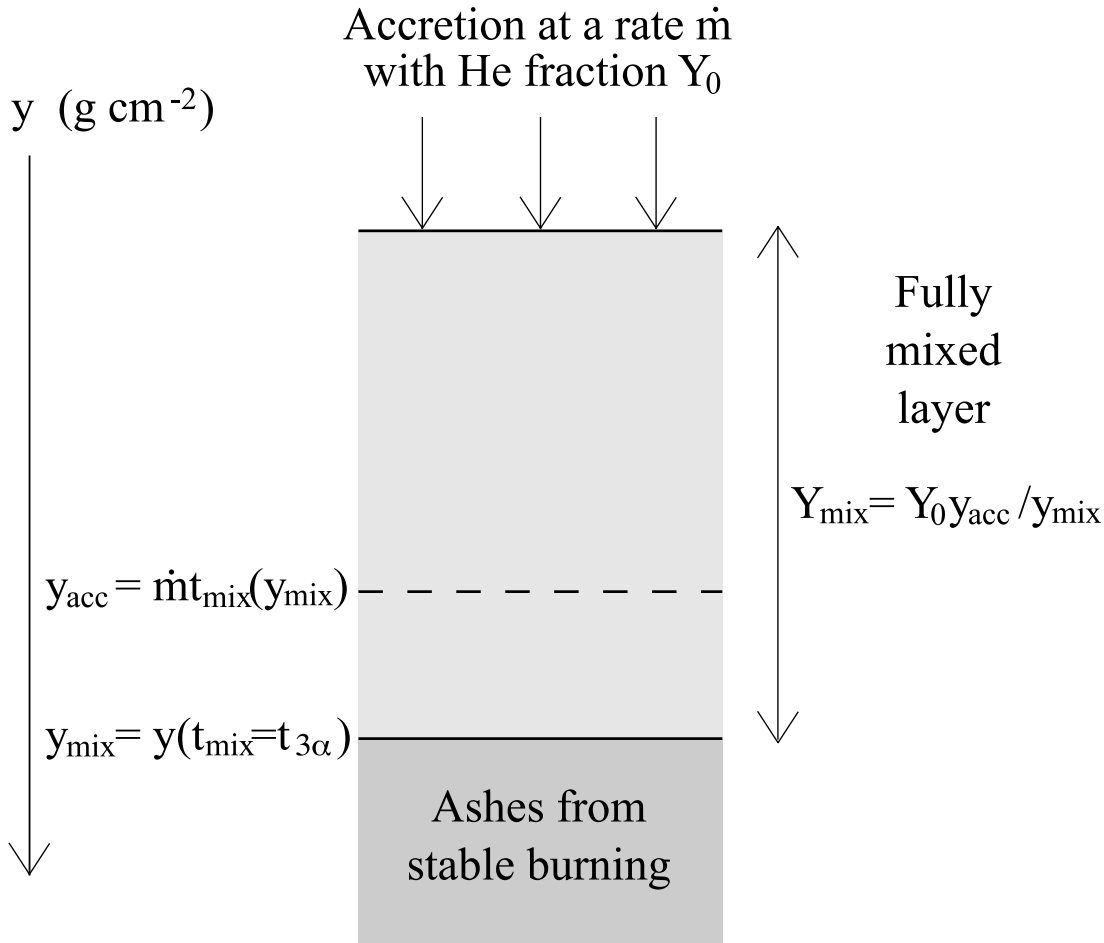$$-\frac{\dot{m}}{\rho} \frac{dY}{dz} = D \frac{d^2 Y}{dz^2} - \frac{Y}{t_{3\alpha}}. \tag{72}$$

Fig. 12.—Diagram demonstrating the main features of steady state mixing and burning. Material can mix further down to where $t_{mix} = t_{3\alpha}$, which defines the depth y_{mix}. During a timescale $t_{mix}(y_{mix})$, the amount of material which has accreted is $y_{acc} = \dot{m}t_{mix}(y_{mix})$. Within the mixed layer, the helium mass fraction is diluted to a new mass fraction of $Y_{mix} = Y_0 y_{acc}/y_{mix}$.

In the limit where $t_{acc} \gg t_{mix}$ that we are interested in, the term on the left-hand side can be dropped. Finally, making the approximation that $\rho D d/dz \approx y/t_{mix}$, we find

$$\frac{dY}{dy} = -\frac{t_{mix}}{t_{3\alpha}}\frac{Y}{y}. \tag{73}$$

This equation mimics the properties we expect from mixing. When mixing is strong $t_{mix}/t_{3\alpha} \ll 1$ and $dY/dy \approx 0$, the composition does not change with depth. At the depth where $t_{mix} \approx t_{3\alpha}$, $dY/dy \approx -Y/y$ and the helium is depleted exponentially. All the helium burns into carbon, so that carbon has a mass fraction $X_{12} = 1 - Y$.

The envelope profiles are found from simultaneously integrating three differential equations: (1) radiative transfer, equation (52); (2) the entropy equation, $dF/dy = -\epsilon_{3\alpha}$; and (3) continuity of helium, equation (73). We integrate using a shooting method, but first we must set three boundary conditions for the flux, temperature, and helium mass fraction. Since all of the accreted helium must burn if the envelope is in steady state, we set the surface flux to $F = Y_0 E_{3\alpha}\dot{m} + F_c$, where $F_c = 150$ keV nucleon^{-1} $\langle \dot{m} \rangle$ (as discussed in § 4.1). The surface temperature is set from the radiative zero solution (Schwarzschild 1958). The helium abundance in the mixed region, Y_{mix}, is an eigenvalue. It is varied until shooting gives the correct base flux of F_c. This is easily found through iteration, since when Y_{mix} is set too large, too much burning occurs, and the base flux is too small (and vice versa for small Y_{mix}).

In Figure 13 we plot a steady state envelope using $Y_0 = 1$, $\dot{m} = 0.3\dot{m}_{Edd}$, $\Omega = 0.1\Omega_K$, and $\alpha_{TS} = 1$. The shooting method demonstrates that the initial helium abundance within the mixed layer is $Y_{mix} = 0.097$. The top panel of Figure 13 shows the temperature profile (thin solid line) and the critical curve for stability where $d\epsilon_{3\alpha}/dT = d\epsilon_{cool}/dT$ (thick dashed line). The bottom panel of Figure 13 shows that the majority of triple-α burning occurs at $\approx 3 \times 10^8$ g cm^{-2} (thick solid line), which is where the helium is depleted. Comparing the middle and bottom panels of Figure 13 shows that the majority of the burning takes place near where $t_{mix} = t_{3\alpha}$ (as required by construction), which is deeper than where $t_{acc} = t_{3\alpha}$ (the normal condition for steady burning).

To make sure the steady state models we find are physically realizable, we must check the thermal stability of the helium burning. In Figure 14 we compare the quantities $d\epsilon_{3\alpha}/d \ln T$ and $d\epsilon_{cool}/d \ln T$ for three different accretion rates. If the cooling derivative is always larger, then the model is thermally stable. We find stable accretion at $\dot{m}$'s considerably less than the stable accretion rate of $\dot{m} \approx 10\dot{m}_{Edd} \approx 2 \times 10^6$ g cm^{-2} s^{-1} expected for pure helium accretion estimated without mixing (Bildsten 1995, 1998a). Models that are found to be stable in this way are plotted as circles in Figure 11 (from § 5.1). Only at large $\dot{m}$ and small Ω are the models found to be stable. If we where to increase α_{TS}, a wider range of the models in Figure 11 become stable.
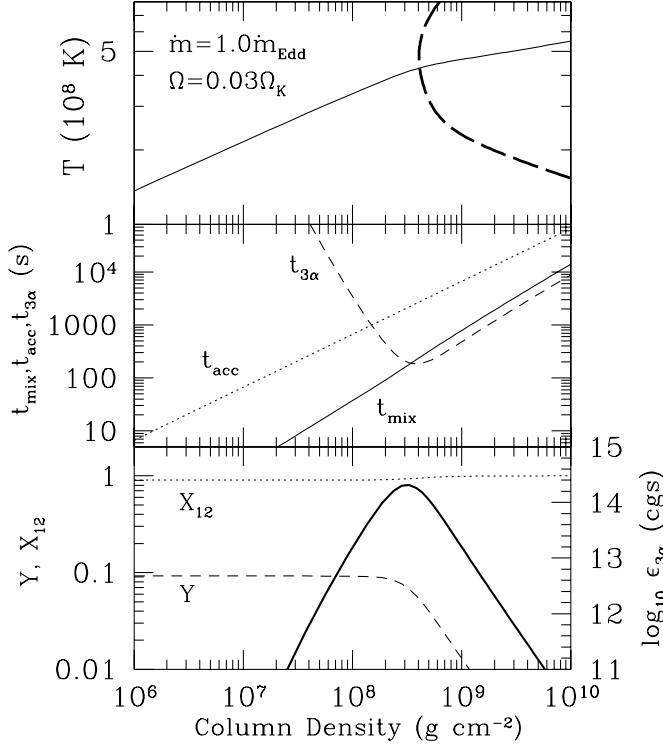
FIG. 13.—Example steady state mixing and burning envelope model using $Y_0 = 1$, $\dot{m} = 1.0\dot{m}_{Edd}$, $\Omega = 0.03\Omega_K$, and $\alpha_{TS} = 1$. The material within the mixed layer has $Y_{mix} = 0.097$. The top panel shows the temperature profile (*solid line*), as well as the critical curve ignition using a helium mass fraction of 0.052 (*thick dashed line*, which is the helium mass fraction at the burning depth). The middle panel compares the key timescales. The bottom panel shows the helium (*dashed line*) and carbon abundances (*dotted line*), as well as the energy generation rate for helium burning (*thick solid line*).

5.4. *The Critical $\dot{m}$ for Stability*

Since we have found a set of models that can stably accrete, mix, and then burn helium, it is interesting to ask what accretion rates and spins are required for this to occur, and how does it depend on parameters such as α_{TS}.

First we must derive the correct condition for stability, including the fact that free-free opacity is important in setting the radiative profile. The one-zone condition for stability at the base of the mixed layer is

$$\frac{d\epsilon_{3\alpha}}{d\ln T} < \frac{d\epsilon_{cool}}{d\ln T}, \qquad (74)$$

where the derivatives are taken at constant pressure. For $\epsilon_{3\alpha} \propto T^\zeta \rho^\chi$, where $\zeta = 44/T_8 - 3$, stability requires (Bildsten 1998a)

$$\zeta - 4 + \frac{\partial \ln \kappa}{\partial \ln T} + \frac{\partial \ln \rho}{\partial \ln T}\left(\chi + \frac{\partial \ln \kappa}{\partial \ln \rho}\right) < 0. \qquad (75)$$

Substituting the scalings for a free-free opacity and ideal gas equation of state, we find $T_8 > 3.26$ is required for stability.

By substituting the analytic form we found for the mixed ignition depth (eq. [67]) into the temperature profile (eq. [61]), we can find the temperature at the base of the mixed layer,

$$T_{ign} = 2.54 \times 10^8 \text{ K } \alpha_{TS}^{0.09} \dot{m}_{0.1}^{0.11} \Omega_{0.1}^{-0.067}. \qquad (76)$$
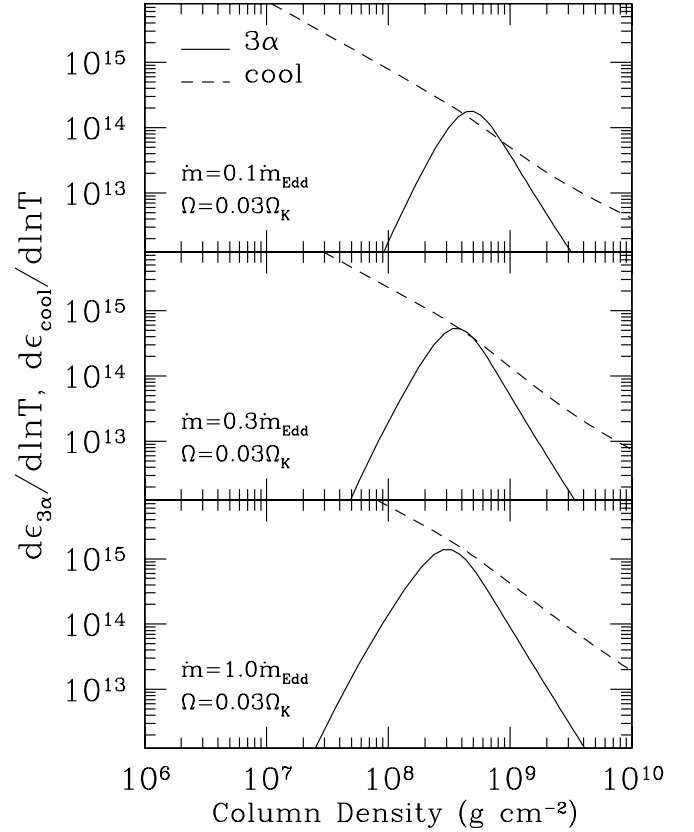

FIG. 14.—Comparison of $d\epsilon_{3\alpha}/d\ln T$ (*solid lines*) and $d\epsilon_{cool}/d\ln T$ (*dashed lines*) as a function of depth for $\dot{m} = 0.1\dot{m}_{Edd}$, $0.3\dot{m}_{Edd}$, and $1.0\dot{m}_{Edd}$ (top to bottom). All the models use $\Omega = 0.03\Omega_K$, $\alpha_{TS} = 1$, and $Y_0 = 1$. This demonstrates that only the $\dot{m} = 1.0\dot{m}_{Edd}$ model is stable out of these three.

By simply asking when $T_{ign} > 3.26 \times 10^8$ K, we derive a stabilizing $\dot{m}$ of

$$\dot{m}_{crit,2} = 1.0\dot{m}_{Edd}\alpha_{TS}^{-0.83}\Omega_{0.1}^{0.62}. \qquad (77)$$

This is in reasonable agreement with Figure 11, which shows stability occurs for $0.9\dot{m}_{Edd} \lesssim \dot{m} \lesssim 1.0\dot{m}_{Edd}$ for $\Omega = 0.1\Omega_K$. It is interesting that $\dot{m}_{crit,2}$ is near (within an order of magnitude) a value where bursts are observed to change. It is conceivable that this mechanism may act to stabilize X-ray bursts for the hydrogen-rich accreting systems, and given the strong scaling $\dot{m}_{crit,2}$ has with α_{TS}, it is possible that more detailed calculations could give results that agree even better with the critical accretion rates that are observed. We discuss this idea in more detail in § 6.

6. DISCUSSION AND CONCLUSION

We have revisited the problem of angular momentum transport in the surface layers of accreting NSs. We found that the hydrodynamic instabilities used by Fujimoto (1993) in a previous study are dwarfed by the magnetic effects of the Tayler-Spruit dynamo. The large viscosity provided by this process results in a very small shear rate and negligible viscous heating. The turbulent mixing is sufficiently large to have important consequences for X-ray bursts. We constructed simple models, both analytic and numerical, to explore mixing for pure helium accretion. From these models we can make a few conclusions that are likely general enough to apply to most viscous mechanisms. As a guide, we
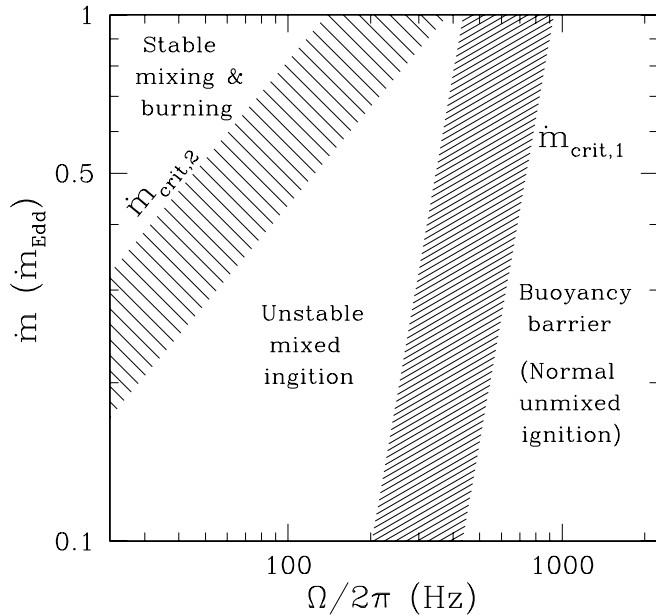
Fig. 15.—Summary of the three regimes of burning found for models including mixing. The boundaries between each regime are shown as shaded regions to emphasize possible uncertainty in the strength of mixing (we consider $\alpha_{TS} = 0.7$–1.5). The heavy shaded region divides where the buoyancy barrier is overcome ($\dot{m}_{crit,1}$, eq. [59]), and the light shaded region divides between stable and unstable mixed burning ($\dot{m}_{crit,2}$, eq. [77]). An additional uncertainty in $\dot{m}_{crit,1}$ is the value of $\Delta \ln \mu$, which could vary depending on the results of previous bursts.

show the different burning regimes we find in Figure 15. These can be summarized as follows.

1. Mixing is strongest at large $\dot{m}$ (when angular momentum is being added at greater rates) and small Ω (which gives a larger relative angular momentum between the NS and accreted material).

2. Mixing has trouble overcoming the buoyancy barrier at chemical discontinuities. But once mixing breaks through this, it extends down to a depth where $t_{mix} = t_{acc}$, which is generally much deeper than the accreted column. This means that mixing should turn on abruptly (as a function of either $\dot{m}$ or Ω). It also means that the importance of mixing depends on the particular ashes left over from previous bursts. If, for example, incomplete burning results in small compositional gradients, mixing would be important in subsequent bursts.

3. Mixing of freshly accreted material with the ashes from previous X-ray bursts can lead to two new effects. First, the layer may ignite, but now in a mixed environment with a short recurrence time of ∼5–30 minutes. Second, if the mixing is strong enough, accreted helium can mix and burn in steady state, quenching X-ray bursts. Both of these regimes have observed analogs, namely, the short recurrence time bursts (e.g., Boirin et al. 2007) and the stabilization of bursting seen at ≈$0.1\dot{m}_{Edd}$ (Cornelisse et al. 2003).

The mixed ignition case can be studied easily using the current numerical experiments (e.g., Woosley et al. 2004) by just artificially accreting fuel with a mixed composition of $Y_{mix} \approx 0.1$–0.6. These calculations are simplified by our conclusion that shearing and heating can be ignored, at least for initial studies. We next conclude by speculating about some of the other ramifications of turbulent mixing.

6.1. Superbursts

An ongoing mystery in the study of bursting NSs is the recurrence times for superbursts, thermonuclear ignition of carbon

in the X-ray burst ashes at columns of ≈10^{11}–10^{12} g cm^{-2} (Cumming & Bildsten 2001; Strohmayer & Brown 2002). This problem could be alleviated by enhanced heating from the core on the order of 1 MeV nucleon^{-1} (Cumming et al. 2006), but this is more than is expected theoretically, even in the newest calculations (Gupta et al. 2007). Shear heating is not large enough to solve this problem, as demonstrated in Figures 3 and 5.

The regime of stable helium burning we have found may, however, create a carbon-rich ocean that would assist in the ignition of superbursts. Carbon fractions of greater than 10% are needed to reproduce the light curves and recurrence times of superbursts (Keek et al. 2006). Calculations of rp-process burning show that *unstable* burning cannot give carbon fractions this high (Schatz et al. 2003). Observationally, in't Zand et al. (2003) showed that the α-value (see § 5.1) is preferentially large for superbursting systems, indicating that some stable burning is occurring, perhaps due to the turbulent mixing we have studied.

6.2. Hydrogen-rich Accretion

One of the main deficiencies of our calculations are the simplified compositions, since most accreting NSs are expected to be accreting a fuel abundant in hydrogen. If the only crucial burning is triple-α, such envelopes can be considered within the framework of our models by using a solar value of $Y_0 = 0.3$. Our models fail, however, when sufficient carbon is produced by triple-α to feedback into hydrogen burning (which burns via the hot-CNO cycle; Hoyle & Fowler 1965). Such a scenario is interesting because it could potentially produce very hydrogen-poor bursts.

In the standard theoretical framework for X-ray bursts, flashes should be hydrogen-poor at low $\dot{m}$ (when there is sufficient time for the hot-CNO cycle to act) and then become mixed hydrogen-helium fuel at higher $\dot{m}$. Paradoxically, observations show a transition at a seemingly universal luminosity of ≈2×10^{37} ergs s^{-1} (approximately $0.1\dot{m}_{Edd}$), but in the opposite sense (Cornelisse et al. 2003). Cooper & Narayan (2006b) argue that their models in fact show this transition (see also Narayan & Heyl 2003), because carbon created during helium simmering increases the hot-CNO rate and the temperature, which decreases the temperature sensitivity of triple-α reactions. To explain the discrepancies between their models and more detailed numerical simulations (Woosley et al. 2004; Heger et al. 2007) requires a decrease in the breakout reactions rate of $^{15}O(\alpha, \gamma)^{19}Ne$ (Cooper & Narayan 2006a; Fisker et al. 2006). Unfortunately, the most recent experimental results do not support a decreased rate (Tan et al. 2007; Fisker et al. 2007). Furthermore, helium accreting systems show this same transition in bursting properties, which is not explained within their framework.

Another idea that may recreate this trend is that the fraction of the star covered by the fuel increases with the *global* accretion fast enough that the *local* accretion rate actually decreases (Bildsten 2000). This can be tested by the recent work of Heger et al. (2007), who claim that the millihertz oscillations observed at around this same universal luminosity of 2×10^{37} ergs s^{-1} (Revnivtsev et al. 2001) are a probe of the local accretion rate where bursting is occurring. The main problem with this suggestion is that it is difficult to understand how the covering of the surface can remain so anisotropic all the way down to the depths of where ignition occurs. Inogamov & Sunyaev (1999) calculated the spreading of accreted material from the equator, where the viscosity is due to a turbulent boundary layer, and find that spreading occurs orders of magnitude shallower in depth than where ignition takes place.

Since mixing gets stronger with $\dot{m}$, it may be that the observed transition is in fact hydrogen being turbulently mixed and burned, analogous to what we have found for pure helium accretion. A possible implication of such an explanation is that slowly spinning NSs are more likely to have their hydrogen depleted, resulting in helium-rich bursts. Assuming that the burst oscillation frequencies are indicative of the NS spin frequency (which is close to true or exactly true for all current explanations: Heyl 2004; Lee 2004; Piro & Bildsten 2005; Payne & Melatos 2006), the systems can be broken into slow spinning ($\sim$300 Hz) and fast spinning ($\sim$600 Hz) classes. This slowly spinning class includes 4U 1916−053 (270 Hz; Galloway et al. 2001), 4U 1702−429 (330 Hz; Markwardt et al. 1999), and 4U 1728−34 (363 Hz; Strohmayer & Markwardt 1999). Do these systems show helium-rich–looking bursts, and if so, is this due to turbulent mixing destroying the hydrogen they are accreting? This can be answered by looking at the recent summary of *RXTE* burst observations by Galloway et al. (2006). 4U 1916−053 has bursts consistent with helium-rich fuel, but this system also has an orbital period of ≈50 minutes (Grindlay et al. 1988). This is an "ultracompact" system in which

the donor is too small to be a hydrogen-rich star, so the accretion is probably helium-rich to begin with. The other two NSs both have bursts with decay times and α-values that suggest helium-rich fuel, which is also supported by model fits to radius expansion bursts from 4U 1728−34 (Galloway et al. 2006). Furthermore, the bursts of 4U 1728−34 look very similar to those of 4U 1820−30 (Cumming 2003), a known ultracompact (see discussion in Podsiadlowski et al. [2002] and references therein).

While it is possible that 4U 1702−429 and 4U 1728−34 have helium-rich donors (and are thus ultracompacts), it may also be that they are accreting hydrogen-rich fuel and show helium-rich bursts because their low spins lead to mixing. As binary parameters of these systems become better known, it will be more clear whether turbulent mixing is indeed needed to explain their burst properties.

APPENDIX

MIXING AND ENERGY CONSERVATION FOR THE TAYLER-SPRUIT DYNAMO

In § 3.1 we summarized the prescriptions that Spruit (2002) provides for the Tayler-Spruit dynamo. The mixing diffusivity is assumed to be equal to the turbulent magnetic diffusivity. Although this is plausible, it is not shown rigorously. Below, we argue that such a scaling is consistent with energy conservation.

Consider a layer differentially rotating with a speed ΔV. The equation for the energy per unit mass expresses the fact that energy from differential rotation can go into either viscous shearing or vertical mixing

$$\frac{d}{dt}\left[\frac{1}{2}(\Delta V)^2\right] = -\frac{1}{2}\nu(q\Omega)^2 - \frac{2\Delta\rho gH}{\rho t_{\text{mix}}}$$
$$= -\frac{1}{2}\nu(q\Omega)^2 - 2N^2D, \quad (A1)$$

where $D = H^2/t_{\text{mix}}$ is the mixing diffusivity. The ratio of the two right-hand terms is called the flux Richardson number (Fujimoto 1988)

$$\text{Rf} = \frac{4N^2D}{\nu(q\Omega)^2} = \frac{4D}{\nu}\text{Ri}, \quad (A2)$$

where $\text{Ri} \equiv N^2/(q^2\Omega^2)$ is the Richardson number. The flux Richardson number is interpreted as the ratio of energy that goes into mixing versus heating (and is usually taken to be $\text{Rf} \sim 0.1$–1). From this result we can solve for the mixing diffusivity

$$D = \frac{\text{Rf}}{4\text{Ri}}\nu. \quad (A3)$$

This matches (up to a factor of order unity, Rf/4) what Spruit (2002) gives for the mixing diffusivity. The factor of Ri in the denominator takes into account the difficulty in overcoming buoyancy to do mixing. The larger the buoyancy, the larger Ri is and the smaller the mixing diffusivity.

REFERENCES

Acheson, D. J. 1978, Philos. Trans. R. Soc. London A, 289, 459
Baker, N., & Kippenhahn, R. 1959, Z. Astrophys., 48, 140
Bhattacharya, D., & van den Heuvel, E. P. J. 1991, Phys. Rep., 203, 1
Bildsten, L. 1995, ApJ, 438, 852
———. 1998a, in The Many Faces of Neutron Stars, ed. R. Buccheri, J. van Paradijs, & A. Alpar (Dordrecht: Kluwer), 419
———. 1998b, ApJ, 501, L89
———. 2000, in AIP Conf. Proc. 522, Cosmic Explosions, ed. S. S. Holt & W. W. Zhang (New York: AIP), 359
Bildsten, L., & Brown, E. F. 1997, ApJ, 477, 897
Bildsten, L., & Cumming, A. 1998, ApJ, 506, 842
Boirin, L., Keek, L., Mendez, M., Cumming, A., in 't Zand, J. J. M., Cottam, J., Paerels, F., & Lewin, W. H. G. 2007, A&A, 465, 559

Braithwaite, J. 2006, A&A, 449, 451
Brown, E. F. 2000, ApJ, 536, 915
———. 2004, ApJ, 614, L57
Brown, E. F., & Bildsten, L. 1998, ApJ, 496, 915
Brown, E. F., Bildsten, L., & Chang, P. 2002, ApJ, 574, 920
Chabrier, G., & Potekhin, A. Y. 1998, Phys. Rev. E, 58, 4941
Chakrabarty, D., Morgan, E. H., Muno, M. P., Galloway, D. K., Wijnands, R., van der Klis, M., & Markwardt, C. B. 2003, Nature, 424, 42
Cooper, R. L., & Narayan, R. 2006a, ApJ, 648, L123
———. 2006b, ApJ, 652, 584
Cornelisse, R., et al. 2003, A&A, 405, 1033
Cumming, A. 2003, ApJ, 595, 1077
Cumming, A., & Bildsten, L. 2000, ApJ, 544, 453

Cumming, A., & Bildsten, L. 2001, ApJ, 559, L127

Cumming, A., Macbeth, J., in't Zand, J. M. M., & Page, D. 2006, ApJ, 646, 429

Cumming, A., Zweibel, E., & Bildsten, L. 2001, ApJ, 557, 958

Denissenkov, P. A., & Pinsonneault, M. 2007, ApJ, 655, 1157

Endal, A. S., & Sofia, S. 1978, ApJ, 220, 279

Fisker, J. L., Görres, J., Wiescher, M., & Davids, B. 2006, ApJ, 650, 332

Fisker, J. L., Tan, W., Görres, J., Wiescher, M., & Cooper, R. L. 2007, ApJ, in press (astro-ph/0702412)

Fricke, K. 1968, Z. Astrophys., 68, 317

Fujimoto, M. Y. 1987, A&A, 176, 53

———. 1988, A&A, 198, 163

———. 1993, ApJ, 419, 768

Fujimoto, M. Y., Hanawa, T., & Miyaji, S. 1981, ApJ, 247, 267

Fujimoto, M. Y., Sztajno, M., Lewin, W. G. H., & van Paradijs, J. 1987, ApJ, 319, 902

Fushiki, I., & Lamb, D. Q. 1987, ApJ, 317, 368

Galloway, D. K., Chakrabarty, D., Muno, M., & Savov, P. 2001, ApJ, 549, L85

Galloway, D. K., Muno, M. P., Hartman, J. M., Savov, P., Psaltis, D., & Chakrabarty, D. 2006, ApJS, submitted (astro-ph/0608259)

Goldreich, P., & Schubert, G. 1967, ApJ, 150, 571

Grindlay, J. E., Bailyn, C. D., Cohn, H., Lugger, P. M., Thorstensen, J. R., & Wegner, G. 1988, ApJ, 334, L25

Gupta, S., Brown, E. F., Schatz, H., Möller, P., & Kratz, K.-L. 2007, ApJ, 662, 1188

Haensel, P., & Zdunik, J. L. 1990, A&A, 227, 431

———. 2003, A&A, 404, L33

Heger, A., Cumming, A., & Woosley, S. E. 2007, ApJ, in press (astro-ph/0511292)

Heger, A., Langer, N., & Woosley, S. E. 2000, ApJ, 528, 368

Heyl, J. S. 2004, ApJ, 600, 939

Hoyle, R., & Fowler, W. A. 1965, in Quasi-Stellar Sources and Gravitational Collapse, ed. I. Robinson, A. Schild, & E. L. Schucking (Chicago: Univ. Chicago Press), 17

Inogamov, N. A., & Sunyaev, R. A. 1999, Astron. Lett., 25, 269

in't Zand, J. J. M., Kuulkers, E., Verbunt, F., Heise, J., & Cornelisse, R. 2003, A&A, 411, L487

Keek, L., in't Zand, J. J. M., & Cumming, A. 2006, A&A, 455, 1031

Lee, U. 2004, ApJ, 600, 914

Lewin, W. H. G., van Paradijs, J., & Taam, R. E. 1995, in X-ray Binaries, ed. W. H. G. Lewin, J. van Paradijs, & E. P. J. van den Heuvel (Cambridge: Cambridge Univ. Press), 175

Lovelace, R. V. E., Kulkarni, A. K., & Romanova, M. M. 2007, ApJ, 656, 393

Maeder, A., & Meynet, G. 2004, A&A, 422, 225

Markwardt, C. B., Strohmayer, T., & Swank, J. 1999, ApJ, 512, L125

Miralda-Escudé, J., Paczyński, B., & Haensel, P. 1990, ApJ, 362, 572

Muno, M. P., Chakrabarty, D., Galloway, D. K., & Psaltis, D. 2002, ApJ, 580, 1048

Muno, M. P., Galloway, D. K., & Chakrabarty, D. 2004, ApJ, 608, 930

Narayan, R., & Heyl, J. S. 2003, ApJ, 599, 419

Paczyński, B. 1983, ApJ, 267, 315

Payne, D. J. B., & Melatos, A. 2006, ApJ, 652, 597

Pedlosky, J. 1987, Geophysical Fluid Dynamics (New York: Springer)

Piro, A. L., & Bildsten, L. 2005, ApJ, 629, 438

Podsiadlowski, P., Rappaport, S., & Pfahl, E. D. 2002, ApJ, 565, 1107

Revnivtsev, M., Churazov, E., Gilfanov, M., & Sunyaev, R. 2001, A&A, 372, 138

Schatz, H., Bildsten, L., Cumming, A., & Ouelette, M. 2003, Nucl. Phys. A, 718, 247

Schatz, H., Bildsten, L., Cumming, A., & Wiescher, M. 1999, ApJ, 524, 1014

Schwarzschild, M. 1958, Structure and Evolution of the Stars (New York: Dover)

Spitzer, L. J. 1962, Physics of Fully Ionized Gases (New York: Interscience)

Spruit, H. C. 1999, A&A, 349, 189

———. 2002, A&A, 381, 923

———. 2006, preprint (astro-ph/0607164)

Strohmayer, T. E., & Bildsten, L. 2006, in Compact Stellar X-Ray Sources, ed. W. H. G. Lewin & M. van der Klis (Cambridge: Cambridge Univ. Press), 113

Strohmayer, T. E., & Brown, E. F. 2002, ApJ, 566, 1045

Strohmayer, T. E., & Markwardt, C. B. 1999, ApJ, 516, L81

Tan, W. P., Fisker, J. L., Görres, J., Couder, M., & Wiescher, M. 2007, Phys. Rev. Lett., submitted

Tassoul, J.-L. 1978, Theory of Rotating Stars (Princeton: Princeton Univ. Press)

Tayler, R. J. 1973, MNRAS, 161, 365

Townsend, A. A. 1958, J. Fluid Mech., 4, 361

van Paradijs, J., Penninx, W., & Lewin, W. H. G. 1988, MNRAS, 233, 437

von Zeipel, H. 1924a, MNRAS, 84, 684

———. 1924b, MNRAS, 84, 665

Wasiutyński, J. 1946, Astrophys. Norvegica, 4, 1

Wijnands, R., & van der Klis, M. 1998, Nature, 394, 344

Woosley, S. E., et al. 2004, ApJS, 151, 75

Yoon, S.-C., & Langer, N. 2004, A&A, 419, 623

Zahn, J.-P. 1992, A&A, 265, 115

Zdunik, J. L., Haensel, P., Paczyński, B., & Miralda-Escudé, J. 1992, ApJ, 384, 129